Quantitative pollen-based paleoclimate reconstructions for the past 18.5 ka in southwestern Yunnan Province, China

Xiayun Xiao, Yan Zhao, Changting Chi, Zhuo Zheng, Chunmei Ma, Chen Liang, Limi Mao, Aubrey Hillman

PII: S0921-8181(23)00261-8

DOI: https://doi.org/10.1016/j.gloplacha.2023.104288

Reference: GLOBAL 104288

To appear in: *Global and Planetary Change*

Received date: 14 December 2022

Revised date: 31 August 2023

Accepted date: 24 October 2023

Please cite this article as: X. Xiao, Y. Zhao, C. Chi, et al., Quantitative pollen-based paleoclimate reconstructions for the past 18.5 ka in southwestern Yunnan Province, China, *Global and Planetary Change* (2023), https://doi.org/10.1016/j.gloplacha.2023.104288

Quantitative pollen-based paleoclimate reconstructions for the past 18.5 ka in southwestern Yunnan Province, China

Xiayun Xiao[a], Yan Zhao[b], Changting Chi[a, c], Zhuo Zheng[d], Chunmei Ma[e], Chen Liang[b], Limi Mao[f], Aubrey Hillman[g]

[a] State Key Laboratory of Lake Science and Environment, Nanjing Institute of Geography and Limnology, Chinese Academy of Sciences, Nanjing 210008, China

[b] Key Laboratory of Land Surface Pattern and Simulation, Institute of Geographic Sciences and Natural Resources Research, Chinese Academy of Sciences, Beijing 100101, China

[c] University of Chinese Academy of Sciences, Beijing 100049, China

[d] Guangdong Provincial Key Laboratory of Geodynamics and Geohazards, School of Earth Sciences and Engineering, Sun Yat–sen University, Guangzhou 510275, China

[e] School of Geographic and Oceanographic Sciences, Nanjing University, Nanjing 210023, China

[f] State Key Laboratory of Palaeobiology and Stratigraphy, Nanjing Institute of Geology and Palaeontology, Chinese Academy of Sciences, Nanjing 210008, China

[g] Department of Atmospheric and Environmental Sciences, University at Albany, State University of New York, Albany 12222, USA

Abstract

Quantitative reconstruction of past climate plays an important role in understanding global and regional climate changes and validating climate models. Although some important progress has been made in quantitative paleoclimate reconstructions based on terrestrial records in the Indian summer monsoon region, high-resolution quantitative studies spanning the last ~20 ka are still relatively sparse with differing results. This study presents high-resolution quantitative variations

in mean temperature of the coldest month (MTCM, the first controlling factor of the regional vegetation), mean annual temperature (MAT, the second controlling factor), and mean annual precipitation (MAP) from Lake Tengchongqinghai in southwestern China, based on an updated modern pollen dataset and the fossil pollen record spanning the last 18.5 ka. The results show that temperature and precipitation increased gradually from 18.5 ka, and peaked from 7.2-4.5 ka when MAT was on average 1.0 °C higher than the modern observational value (14.5 °C), corresponding to the mid-Holocene climatic optimum, and then decreased gradually. The total reconstructed ranges are between -2.2 and 9.2 °C for MTCM, 7.7 and 17.2 °C for MAT, and 840 and 1300 mm for MAP. On top of this overall climate trend, seven abrupt cold and dry events were detected during the periods of 16.2-14.8 ka, 12.8-11.5 ka, ~11.1 ka, 9.1-8.4 ka, ~7.7 ka, 4.3-3.7 ka, and 0.68-0.009 ka (1270-1950 CE). The results of this quantitative reconstruction were validated by both statistical and ecological evaluations. We conclude that the trend of climatic change since 18.5 ka in this study area was primarily driven by June, July, August, and September solar insolation and changes in radiative forcing and greenhouse gas concentrations. The abrupt changes may be caused by changes in the Atlantic meridional overturning circulation, solar activity, the position of the Intertropical Convergence Zone, and volcanic activity.

Keywords: Pollen; Quantitative reconstruction; Temperature and precipitation; Abrupt events; Indian summer monsoon; Since the last deglaciation; Southwestern China

1. Introduction

Quantitative paleoclimate reconstruction has always been the core goal of paleoclimatology research and drives paleoclimatology innovation. It plays an important role in understanding the

laws of past global and regional climate changes and in reducing the uncertainty of future climate change prediction (Wright et al., 1993; Joussaume and Teylor, 1995; IPCC, 2013). Pollen has long been considered as a powerful proxy for quantitative paleoclimate reconstruction based on modern relationships between pollen and climate (Webb and Bryson, 1972; Davis, 2003; Seppä et al., 2004; Chevalier et al., 2020). Robust pollen-based climate reconstructions are mainly controlled by the quality of the modern pollen and climate variable calibration sets, the spatial extent of the calibration sets, the sensitivity of vegetation to climate variables, and the selection of reconstructed climate indicators and appropriate numerical approaches (Birks et al., 2010; Cao et al., 2017; Chevalier et al., 2020; Zhao Y et al., 2021). However, due to the restriction of various factors such as database quantity and quality, computer techniques and statistical methods, most of early studies of pollen-based quantitative paleoclimate reconstruction quantitatively reconstructed the subjectively selective climate factors based on database owned by researchers by using one or two quantitative reconstruction methods with no statistical validation. Therefore, there is uncertainty regarding the reliability of the reconstructions. Recently, the number of modern pollen sites has rapidly increased, filling in many spatial gaps, and the quality of modern pollen databases has been significantly improved. With the development of computer techniques and statistical methods, the methods and systems of pollen-based quantitative paleoclimate reconstruction are becoming increasingly mature (Chevalier et al., 2020; Liang et al., 2020; Zhao Y et al., 2021). Therefore, in order to reliably and quantitatively reconstruct climate, it is necessary to perform modern pollen data screening, carefully select calibration sets, perform major climate factor analysis, select appropriate models, and assess results using statistics and ecologies.

The Indian summer monsoon (ISM) intensively impacts human activity and economic

development in the regions adjacent to the Himalayas and Tibetan Plateau (TP) where approximately 75% of the world's population lives (Overpeck et al., 1996; Benn and Owen, 1998), making it of great scientific importance. Southwestern China is in close proximity to the TP, and strongly affected by the ISM, making it a key region to reconstruct paleoclimate changes and environmental effects from the ISM. Over the past ~20 ka, the global climate has experienced an overall warming trend from the Last Glacial Maximum (LGM) to the Holocene thermal maximum (HTM), followed by a general cooling trend. During this interval, a series of millennial- and centennial- scale abrupt events characterized by rapid warming or cooling occurred in the Northern Hemisphere (NH), such as the Heinrich Event 1 (H1, ~17.5 to 16.0 ka) and the associated Oldest Dryas cold period (~18.0 to 14.7 ka), the Bølling/Allerød warm period (B/A, ~14.7 to 12.9 ka), the Younger Dryas cold event (YD, ~12.9 to 11.7 ka) (Alley and Clark, 1999; Shakun and Carlson, 2010), the 8.2 ka and 4.2 ka cold events, the Medieval Warm Period (MWP), and the Little Ice Age (LIA) et al. (Bond et al., 1997; Wang et al., 2005; Mann et al., 2009). Thus this interval covers a wide range of warming/cooling events and increase/decrease in precipitation of different amplitude and rates. Accurate quantitative reconstruction of paleoclimate over the past 20 ka also allows us to explore the response of past ecosystems, which facilitates a comprehensive understanding of climate change mechanisms and consequences.

Early quantitative paleoclimate reconstructions mainly focused on sea surface temperatures (SSTs) in the ISM region (Sonzogni et al., 1998; Kudrass et al., 2001; Naidu and Malmgren, 2005; Huguet et al., 2006; Govil and Naidu, 2010; 2011; Mohtadi et al., 2014) and in recent years quantitative paleoclimate reconstructions based on terrestrial records have rapidly increased (Shen et al., 2006, 2008; Lu et al., 2011; Herzschuh et al., 2014; Opitz et al, 2015; Wu et al., 2018;

Zhang et al., 2017; 2019; Tian et al., 2019; Liang et al., 2020; Sun et al., 2021; Wang et al., 2021; Yan et al., 2021; Zhao C et al., 2021; Zhao Y et al., 2021; Zhang C et al., 2022). However, there are still relatively few high-resolution terrestrial quantitative paleoclimate records that span the last ~20 ka. Moreover, the reconstructed climatic factors are also not the same, such as: July temperature based on subfossil chironomids (Zhang et al., 2017; 2019), mean annual temperature (MAT) and temperature in ice-free seasons based on branched glycerol dialkyl glycerol tetraethers (brGDGTs) (Tian et al., 2019; Zhao C et al., 2021; Wang et al., 2021; Yan et al., 2021), and MAT, mean temperature of the warmest month (MTWM), and mean annual precipitation (MAP) based on pollen (Herzschuh et al., 2014; Opitz et al, 2015; Zhao Y et al., 2021), etc. Among these published studies, even quantitative reconstruction results for the same climate factor based on the same proxy differed greatly. For example, MAT results based on brGDGTs since 20 ka from Lake Tengchongqinghai showed that the range reconstructed by Tian et al. (2019) was between 11.9 and 15.6 °C, but was 15.2 and 19.2 °C for Zhao C et al. (2021). Quantitative reconstructions of precipitation are fewer, while change of precipitation is more complex and regional than temperature. Thus, it is urgent to strengthen the quantitative paleoclimate reconstruction including temperature and precipitation based on different proxies in the ISM region over the past ~20 ka.

This study reconstructs quantitatively reliable sequences of climate variables spanning the last 18.5 ka from southwestern China based on pollen data, using the comprehensive framework for pollen-based quantitative reconstruction approaches established by Liang et al. (2020). Our objectives are to: (1) identify the main climate control on vegetation change at different spatial extents around the study area; (2) provide high-resolution and reliable quantitative sequences of temperature and precipitation for the ISM region since 18.5 ka; (3) explore mechanisms of climate

change by comparing the results of the quantitative reconstruction with climate forcings and by performing cross correlation, wavelet coherence, and spectral analysis.

2. Study area

Lake Tengchongqinghai (25°7'56.75" N，98°34'19.16" E, 1885 m a.s.l.) is a small crater lake located in the Hengduan Mountains at the southeastern margin of the TP (Fig. 1a). It is hydrologically recharged by precipitation, surface runoff and groundwater, without a natural outflow at present (Wang et al., 2002). The study region is characterized by a subtropical humid monsoon climate. It is mainly affected by the warm-humid airflow from the Indian Ocean and Bengal Bay in the summer and by the southern branch of the westerly airflow in the winter. The climate in the region is warm and very humid in summer and mild and moderately dry in winter. MAT at the Tengchong meteorological station (25º 01′ N, 98 º 30′ E, 1654 m a.s.l.) about 15 km away from Lake Tengchongqinghai is 15.4 ℃ (based on data from 1981 to 2010 downloaded from China Meteorological Administration. http://data.cma.cn), with average monthly temperatures in July and January of 19.8 ℃ and 8.6°C, respectively. The MAP is 1506 mm, with an average of 19.9 mm in January and 291.3 mm in July, and most of the precipitation (85%) is concentrated in the May to October period (Xiao et al., 2015).

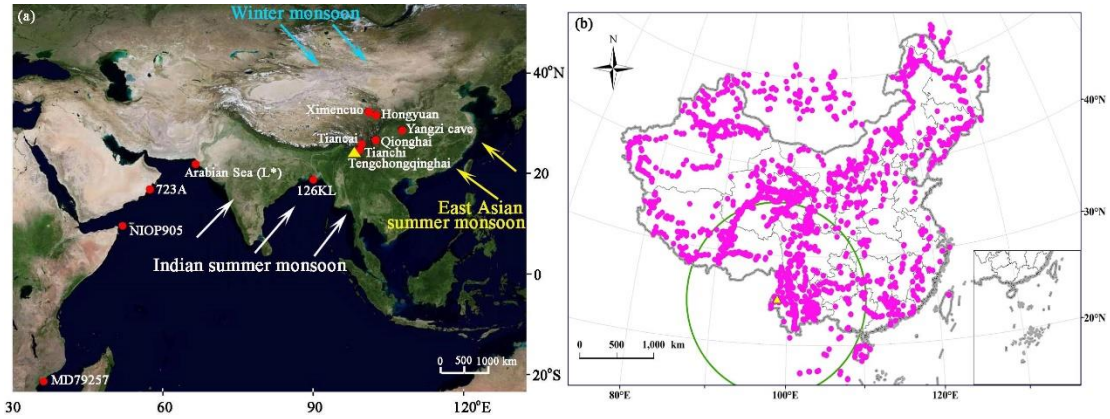

Fig. 1. (a) Location map of Lake Tengchongqinghai (yellow triangle) from southwestern China and monsoon

pathways. Other sites (red circles) located in the Indian summer monsoon region and mentioned in Section 5.2 are also shown. (b) The sample sites of the modern pollen calibrate set. The sample sites in the green circle with a 1200 km radius around core TCQH1 (yellow triangle) form the selected calibration set.

Vegetation in Yunnan Province is the most abundant in China, and vertical vegetation belts flourish. Vegetation belts range from tropical monsoon rain forest to sparse alpine regions in a less than 600 km region between Xishuangbanna and the Yulong Mountains; this mimics global vegetation type distribution (Compiling Group of Yunnan Vegetation, 1987). The regional vegetation around Lake Tengchongqinghai is semi-humid evergreen broadleaved forest, mainly composed of *Castanopsis delavayi* and *Lithocarpus* spp., accompanied by other trees such as *Pinus yunnanensis*, *P. armandii*, *Alnus nepalensis*, and *Vixbucklandia populnea*. Due to the strong disturbances of human activities, the vegetation in the catchment of the lake is mainly composed of artificial monoculture forests such as *Taiwania cryptomerioides*, *Cunninghamia lanceolata* and *A. nepalensis* at present (Xiao et al., 2015).

3. Materials and methods

3.1. Materials

3.1.1. Fossil pollen record

A high-resolution pollen record spanning the last 18.5 ka from Lake Tengchongqinghai (core TCQH1) was used for quantitative reconstruction. From 278 samples, a total of 241 pollen types were identified. Its detailed chronology, pollen sequence, and vegetation history have been presented and discussed qualitatively in a prior publication (Xiao et al., 2015). A brief description of the pollen record and comparison with the other two pollen records in the same lake are shown in the supplemental files (SI Text). In this record, *Quercus* (evergreen) include *Quercus*

semicarpifolia type (or *Quercus* sect. *Heterobalanus*, commonly called alpine oaks) and *Cyclobalanopsis* type (or *Quercus* sect. *Cyclobalanopsis*) due to morphologically indistinguishable under light microscopy (LM). However, their ecological characteristics are significantly different. *Quercus semicarpifolia* type has 9-11 species and is concentrated in the Himalayas-Hengduan Mountains (Zhou et al., 2007), which is mainly distributed at the higher altitude regions (>2600 m a.s.l.) with relatively cold climatic conditions. The *Cyclobalanopsis* type is mostly distributed at the lower altitude regions (<2600 m a.s.l.) with relatively warm climatic conditions in southwestern China (Huang et al., 1998). Because only percentages of pollen types are considered in quantitative reconstruction, unlike in qualitative analysis, the overall characteristics of pollen assemblage are considered. Combining *Quercus semicarpifolia* with *Cyclobalanopsis* as *Quercus* (evergreen) has a disproportionately large impact on quantitative reconstructions, which may lead to inaccurate results. In order to solve this problem, we performed a scanning electron microscopy (SEM) analysis of the fossil samples to classify *Quercus* pollen grains into three types (*Quercus* (deciduous), *Quercus semicarpifolia* type and *Cyclobalanopsis* type) (SI Text). The pollen percentages of *Quercus* (deciduous), *Quercus semicarpifolia* type, *Cyclobalanopsis* type and the other major pollen taxa are presented in the pollen diagram (Fig. 2).

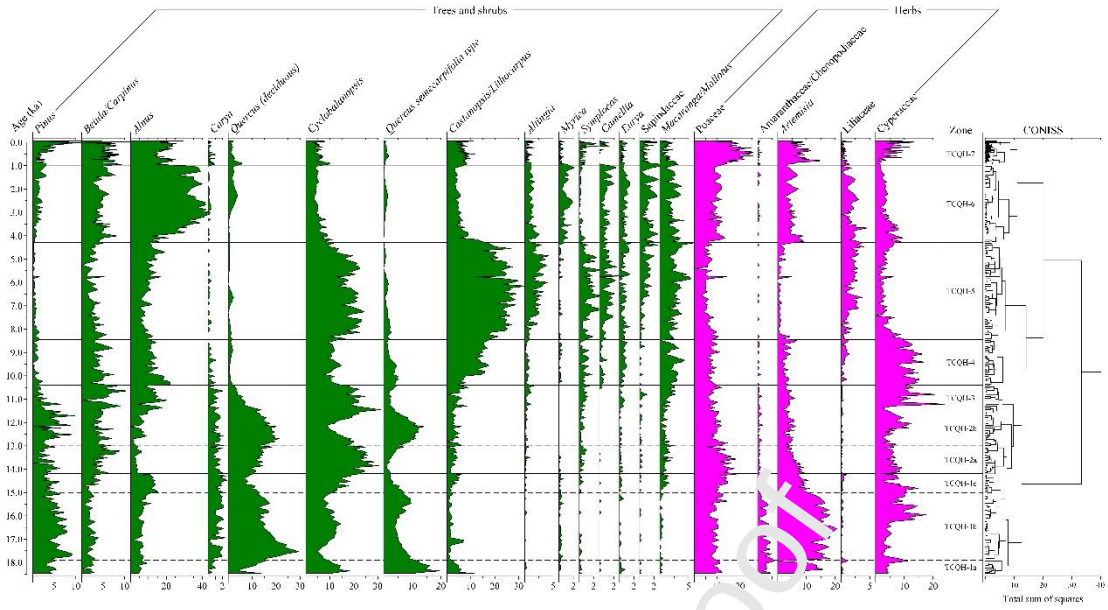

Fig. 2. Pollen percentage diagram of the major taxa from Lake Tengchongqianghai.

3.1.2. Modern pollen dataset

For the quantitative reconstruction we used an updated modern pollen dataset comprising 4258 samples (Figure 1b) based on Liang et al. (2020)'s 3133 samples and 1125 new samples mainly concentrating in southwestern China. This dataset included 525 terrestrial pollen types. In order to obtain a high-quality calibration set, we first deleted 43 samples with <100 pollen grains and 16 samples from aiport, 127 samples with potential outliers identified using hierarchical cluster (H-cluster) analysis, and 107 samples strongly influenced by human activity. 3965 samples remained and acted as the calibration set for our quantitative reconstruction. 525 terrestrial plant pollen types were merged into 241 pollen types according to the fossil pollen dataset. *Quercus semicarpifolia* and *Cyclobalanopsis* are the two types of *Quercus* (evergreen) which are the major tree species in southwestern China; they were not distinguished in our modern pollen dataset due to their similar morphological characteristics. We can only classify roughly *Quercus* (evergreen) into *Quercus semicarpifolia* type (*Quercus* (evergreen) distributed above 2600 m a.s.l.) and

Cyclobalanopsis type (*Quercus* (evergreen) distributed below 2600 m a.s.l.) according to their altitudinal distribution range.

3.1.3. Modern climate data

The climatic parameters for modern pollen sample sites are necessary database for quantitative reconstruction. Here, we selected seven meteorological parameters including MAT, MTWM, mean temperature of the coldest month (MTCM), MAP, mean precipitation of the warmest month (MPWM), mean precipitation of the coldest month (MPCM), and growing degree days above 5 °C (GDD5). The thin plate spline regression (Hijmans et al., 2005) was applied to interpolate the modern climate data of the 3965 sample sites from 756 stations across China for the interval of 1981–2010, using the R package Fields (Nychka et al., 2020).

3.2. Methods

3.2.1. Reconstruction models and calibration sets

In this study, 5 models including Weighted Average with inverse deshrinking (WA. inv), Weighted averaging partial least squares (WAPLS), Modern Analogue Technique (also known as the best analogue method, in order not to confuse the abbreviations of mean annual temperature (MAT), we adopted BAM as the abbreviated form of Modern Analogue Technique), Locally-Weighted Weighted-Averaging (LWWA) and Locally-Weighted Weighted-Averaging partial least squares (LWWAPLS) were used to perform quantitative reconstruction. For the transfer function models (WA, WAPLS), two methods were used to select an appropriate range of modern pollen calibration set. One is based on geographical distance within a series of radii (500, 800, 1000, 1200, 1300, 1400, 1500, 1800, 2000 km, and all dataset) of the modern sites around the core site (Cao et al., 2017). The other is to select a certain number (k=10, 15, 20, 25, 30, 35, 40, 45,

50, 60, 80, and 100) of modern analogues for each fossil sample and combine these analogues into a calibration set (Liang et al., 2020). For the BAM model, the dissimilarity between each fossil sample and the modern samples is defined by the minimum squared chord distance (SCD) (Birks et al., 2012). The value of k (number of analogues) was chosen based on the lowest root mean squared error (RMSE) via cross-validation method. In LWWA and LWWAPLS models, a dynamic calibration set was established based on the several closest analogues for each fossil sample separately (Birks, 2012; Liang et al., 2020). Numerical comparisons were employed among different number of k (10, 15, 20, 25, 30, 35, 40, 45, 50, 60, 80, and 100), which is similar to the selection process of BAM.

3.2.2. Main climatic controlling factors for the calibration sets with different spatial extent

The determination of main climatic controlling factors for regional vegetation is a prerequisite for accurately quantitative reconstruction of paleoclimate. Prior to the quantitative reconstruction, relationships between modern pollen data and climatic variables were assessed by ordination techniques, based on the square root transformed pollen data (144 pollen taxa with their percentages ≥ 1% in at least 10 samples). To check the underlying linearity of the pollen data, a detrended correspondence analysis (DCA) was initially carried out. The gradient lengths of the first axis in DCA were all >3.0 standard deviation (SD) for the calibration sets with different spatial extents, indicating that a unimodal-based Canonical correspondence analysis (CCA) was appropriate for exploring species-environment relationships (ter Braak and Šmilauer, 2012). To test the explanatory potential of the climatic variables, a series of constrained CCAs are run with each climatic variable separately using forward selection (999 Monte-Carlo permutations; $P \leq 0.05$) (ter Braak, 1988). The ratio of the first constrained eigenvalue (λ_1) to the first unconstrained

eigenvalue (λ_2) for each climatic variable was used to evaluate which climatic variables with a high λ_1/λ_2 ratio can be potentially reconstructed (ter Braak, 1988; Juggins, 2013). Pearson correlation coefficients between the climate variables and the variance inflation factors (VIF) derived from CCA were used to check collinearity relationships among variables (Juggins and Birks, 2012). Variables with a large VIF (>20) indicate high multicollinearity with other climatic variables and do not bring any unique contribution to the explanatory power of all variables (ter Braak and Prentice, 1988). All these ordination analyses were performed using statistical program CANOCO version 5.0 (ter Braak and Šmilauer, 2012).

3.2.3. Result evaluation and validation

Evaluating a reconstruction is a complex process that relies on both statistical indicators and expert knowledge (Chevalier et al., 2020). Here, five methods (coverage of fossil taxa in modern calibration set, a goodness-of-fit analysis, cross-validation, significant test and ecological explanation) were applied to assess reliability of the quantitative reconstruction results (SI Text). This evaluation process is more advantageous than the traditional technique which only assesses model performance.

All of the above analyses except for CCA were employed in software R (version 3.6.0). Package "rioja" was used for WA, WAPLS, BAM, LWWA, and LWWAPLS models, and package "PalaeoSig" was used for significant test. Cross correlation and spectral analysis adopted later were performed in PAST software version 4.11 (Hammer et al., 2001), and wavelet coherence was performed with a Matlab software package (wavelet-coherence-master) by Grinsted et al. (2004). The improved ensemble empirical mode decomposition with adaptive noise (ICEEMDAN) was carried out in MatLab using code provided by Colominas et al. (2014).

4. Results

4.1. Identification of main climatic controlling variable(s) and selection of reconstruction model and calibration set

The explanatory potential results of seven selected climatic variables as sole predictor for the calibration sets with different spatial extents showed that: 1) MAP was the first controlling factor for the calibration sets with radii larger than 1300 km, 2) MTCM was the first controlling factor for the calibration sets with radii between 1300 and 1000 km, and 3) GDD5 was the first controlling factor for the calibration sets with radii less than 1000 km (Table 1). The numerical performance of all the models in the different calibration sets for MTCM and MAP was calculated based on leave-one-out cross validation and summarized in Table 2. The results indicate that the BAM model shows the lowest RMSEP and higher R^2 for MTCM and MAP, however, their reconstruction results indicate "flatter" profiles and abnormal features of climate change (Fig. S1), which may be 'noisy' reconstructions because the models exhibit too much local structure in the calibration set due to spatial autocorrelation (Telford and Birks, 2005; Zhao Y et al., 2021). After removing the BAM model, the values of RMSEP, R^2, the RMSEP as a percentage of the climatic gradient range of the calibration set, and the ratio of change in RMSEP to change in R^2 (relative to the lowest RMSEP for the WAPLS model in the calibration set with a 500 km spatial extent) were comprehensively compared, and then the WAPLS model and the calibration set with a 1200 km spatial extent were selected as the most reliable model and the most appropriate calibration set for final climate reconstruction. For the selected calibration set with a 1200 km spatial extent, the first controlling factor is MTCM, then MAT, GDD5, and MAP.

Table 1 Explain powers of climatic variables as sole predictor

Calibration-set radius (km)/Climatic variables	MAT	MTWM	MTCM	GDD5	MAP	MPWM	MPCM	p-value
all data	3.9	2.5	4.5	3.7	5.3	5.2	3.4	0.002
<2000	4.2	3.3	4.9	4	5	4.9	3.2	0.002
<1800	4.3	3.4	4.9	4.2	5	5	3.1	0.002
<1500	4.5	3.7	4.9	4.3	5	4.9	3.3	0.002
<1400	4.5	3.7	4.8	4.2	5	4.9	3.5	0.002
<1300	4.6	3.9	5	4.4	5	4.9	3.3	0.002
<1200	4.7	4.2	4.8	4.5	4.4	4	3.3	0.002
<1000	4.1	3.8	4.1	4.1	3.5	2.8	2.7	0.002
<800	4.4	4.2	4.5	4.6	3.5	2.6	2.9	0.002
<500	4.3	4.1	4.4	4.5	4	3.8	2.6	0.002

Red highlights indicate the highest explanatory power, and gray highlights indicate the lowest explanatory power.

Table 2 Error estimates (RMSEP) of mean temperature of the coldest month (MTCM, ºC) and mean annual precipitation (MAP, mm) for various reconstruction models. The calibration sets were chosen on distance range or by the modern analogue approach.

			MTCM						MAP					
Model	Parameter	Sample number	analog./comp.*1	RMSEP	R^2	the ratio*^{2}	gradient (ºC)	RMSEP % of grad*3	analog./comp.*1	RMSEP	R^2	the ratio*^{2}	gradient (mm)	RMSEP % of grad*3
BAM	500 k	10	k=5	2.0	0.		-12.	6.7	k=5	10	0.		560	7.3

	m	30		1	91		6-17.3	2		4	82		-1970	6
	800 km	1344	k=2	2.23	0.90		-14.6-18.7	6.69	k=5	108	0.79		349-1970	6.63
	1000 km	1542	k=4	2.46	0.90		-17.5-19.7	6.62	k=5	113	0.81		348-1970	6.96
	1200 km	1859	k=4	2.66	0.91		-19.3-19.7	6.82	k=5	112	0.86		296-1970	6.69
	1300 km	2051	k=4	2.80	0.90		-19.3-23.1	6.61	k=5	113	0.88		48-1971	6.18
	1400 km	2372	k=3	2.61	0.91		-19.3-24.0	6.02	k=5	115	0.91		48-1971	5.99
	1500 km	2459	k=4	2.90	0.89		-25.3-25.0	5.76	k=4	140	0.88		37-1971	7.24
	1800 km	2731	k=4	2.85	0.90		-25.3-25.0	5.67	k=4	154	0.88		20-2033	7.65
	2000 km	2908	k=5	2.91	0.89		-25.3-25.0	5.79	k=5	163	0.89		20-2047	8.03
	All dataset	3965	k=5	3.7[illegible]	0.88		-29.6-41.3	5.23	k=6	155	0.90		20-2047	7.66
WA.inv	500 km	1030		3.38	0.74	-0.59	-12.6-17.3	11.32		145	0.64	-1.13	560-1970	10.31
	800 km	1344		3.65	0.74	-0.33	-14.6-18.7	10.95		152	0.58	-1.50	349-1970	9.39
	1000 km	1542		3.81	0.76	-0.16	-17.5-19.7	10.23		153	0.65	-0.38	348-1970	9.46
	1200 km	1859		4.19	0.76	-0.08	-19.3-19.7	10.75		160	0.72	0.34	296-1970	9.57
	1300 km	2051		4.42	0.75	-0.11	-19.3-23.1	10.42		167	0.75	0.49	48-1971	8.70

1400 km	2372	4.56	0.73	-0.15	-19.3-24.0	10.53	191	0.76	0.28	48-1971	9.94
1500 km	2459	4.48	0.74	-0.12	-25.3-25.0	8.91	194	0.77	0.30	37-1971	10.04
1800 km	2731	4.44	0.74	-0.12	-25.3-25.0	8.82	222	0.76	0.18	20-2033	11.02
2000 km	2908	4.42	0.74	-0.13	-25.3-25.0	8.79	235	0.76	0.16	20-2047	11.60
All dataset	3965	6.16	0.65	-0.17	-29.6-41.3	8.69	230	0.78	0.22	20-2047	11.37
10-analogue	140	3.63	0.68	-0.68	-16.2-15.2	11.51	220	0.72	0.09	106-1888	12.36
15-analogue	184	3.73	0.69	-0.57	-18.8-15.2	10.97	219	0.73	0.11	54-1888	11.95
20-analogue	232	3.96	0.71	-0.34	-19.8-15.2	11.31	217	0.74	0.14	54-2025	11.01
25-analogue	271	4.02	0.71	-0.29	-19.8-19.2	10.31	212	0.75	0.18	54-2025	10.74
30-analogue	290	4.14	0.70	-0.32	-19.8-19.2	10.62	220	0.73	0.12	54-2033	11.12
35-analogue	318	4.17	0.71	-0.26	-23.7-19.2	9.73	223	0.74	0.13	54-2033	11.28
40-analogue	347	4.17	0.70	-0.30	-23.7-21.6	9.21	231	0.72	0.08	54-2033	11.66
45-analogue	382	4.20	0.71	-0.27	-23.7-24.0	8.74	234	0.71	0.06	37-2047	11.66
50-analogue	422	4.40	0.70	-0.26	-23.7-24.0	9.23	233	0.71	0.06	20-2047	11.51
60-analogu	472	4.46	0.7	#REF	-23.7-25	9.16	239	0.7	0.05	20-204	11.77

	e				0	!	.0				1		7		
	80-analogue	564		4.45	0.72	#REF!	-23.7-25.0	9.15		237	0.71	0.05	20-2047	11.69	
	100-analogue	654		4.49	0.73	-0.17	-23.9-25.0	9.18		239	0.70	0.04	20-2047	11.81	
WAP LS	500 km	1030	2	3.05	0.79		-12.6-17.3	10.21	2	138	0.68		560-1970	9.81	
	800 km	1344	2	3.32	0.78	-0.05	-14.6-18.7	9.97	2	143	0.64	-1.99	349-1970	8.83	
	1000 km	1542	2	3.40	0.81	0.21	-17.5-19.7	9.15	2	143	0.70	0.95	348-1970	8.81	
	1200 km	1859	3	3.35	0.85	0.81	-19.3-19.7	8.59	2	142	0.78	4.96	296-1970	8.49	
	1300 km	2051	3	3.51	0.84	0.48	-19[illegible].1	3.27	2	153	0.79	1.52	48-1971	7.96	
	1400 km	2372	2	3.88	0.80	0.08	-19.3-24.0	8.96	2	173	0.80	0.71	48-1971	8.97	
	1500 km	2459	3	3.[illegible]0	0.84	0.35	-25.3-25.0	7.14	2	173	0.81	0.75	37-1971	8.97	
	1800 km	2731	3	3.56	0.84	0.36	-25.3-25.0	7.09	2	197	0.81	0.43	20-2033	9.81	
	2000 km	2908	3	3.57	0.83	0.33	-25.3-25.0	7.11	2	212	0.81	0.34	20-2047	10.45	
	All dataset	3965	3	4.86	0.79	0.00	-29.6-41.3	6.85	2	208	0.82	0.41	20-2047	10.25	
	10-analogue	140	2	3.16	0.76	-0.93	-16.2-15.2	10.07	2	197	0.77	0.32	106-1888	11.04	
	15-analogue	184	2	3.19	0.77	-0.45	-18.8-15.2	9.39	2	194	0.79	0.37	54-1888	10.59	
	20-an	23	2	3.2	0.	0.1	-19.	9.3	2	19	0.	0.	54-	9.7	

	alogue	2		9	80	9	8-15.2	9		2	79	42	2025	4
	25-analogue	271	2	3.41	0.79	0.08	-19.8-19.2	8.74	2	187	0.80	0.50	54-2025	9.50
	30-analogue	290	2	3.59	0.77	-0.11	-19.8-19.2	9.20	2	196	0.79	0.36	54-2033	9.93
	35-analogue	318	2	3.65	0.78	-0.05	-23.7-19.2	8.50	2	195	0.80	0.41	54-2033	9.88
	40-analogue	347	2	3.62	0.78	-0.08	-23.7-21.6	7.99	2	203	0.78	0.32	54-2033	10.26
	45-analogue	382	2	3.58	0.79	0.01	-23.7-24.0	7.51	2	206	0.78	0.29	37-2047	10.26
	50-analogue	422	2	3.81	0.77	-0.07	-23.7-24.0	7.98	2	206	0.78	0.28	20-2047	10.17
	60-analogue	472	2	3.87	0.77	-0.07	-23.7-25.0	7.96	2	213	0.77	0.22	20-2047	10.52
	80-analogue	564	2	3.78	0.80	0.06	-23.7-25.0	7.76	2	211	0.77	0.24	20-2047	10.39
	100-analogue	654	2	3.74	0.81	0.12	-23.9-25.0	7.65	2	211	0.77	0.25	20-2047	10.39
LW-WA	k=10	3965		3.81	0.87	0.41	-16.2-15.2	12.15		157	0.90	2.39	106-1888	8.80
	k=15	3965		3.75	0.87	0.47	-18.8-15.2	11.02		155	0.90	2.71	54-1888	8.44
	k=20	3965		3.85	0.87	0.38	-19.8-15.2	11.00		158	0.90	2.21	54-2025	8.02
	k=25	3965		3.89	0.86	0.35	-19.8-19.2	9.97		161	0.90	1.93	54-2025	8.15
	k=30	3965		3.88	0.86	0.36	-19.8-19.2	9.94		160	0.90	1.98	54-2033	8.09

	k=35	3965	3.89	0.86	0.35	-23.7-19.2	9.08	161	0.90	1.92	54-2033	8.12
	k=40	3965	3.97	0.86	0.29	-23.7-21.6	8.77	162	0.89	1.77	54-2033	8.21
LW-WA	k=45	3965	3.98	0.86	0.29	-23.7-24.0	8.34	164	0.89	1.63	37-2047	8.16
	k=50	3965	4.00	0.86	0.28	-23.7-24.0	8.38	167	0.89	1.45	20-2047	8.23
	k=60	3965	4.05	0.85	0.25	-23.7-25.0	8.31	168	0.89	1.40	20-2047	8.27
	k=80	3965	4.18	0.84	0.19	-23.7-25.0	8.58	170	0.88	1.29	20-2047	8.38
	k=100	3965	4.27	0.84	0.15	-23.7-25.0	8.73	175	0.88	1.06	20-2047	8.64
LW-WAPLS Component-ent 2	k=10	3965	3.90	0.86	0.33	-16.2-15.2	12.42	162	0.89	1.80	106-1888	9.09
	k=15	3965	3.90	0.86	0.28	-18.8-15.2	11.73	166	0.89	1.49	54-1888	9.07
	k=20	3965	3.95	0.86	0.31	-19.8-15.2	11.28	166	0.89	1.49	54-2025	8.43
	k=25	3965	3.97	0.86	0.29	-19.8-19.2	10.18	166	0.89	1.53	54-2025	8.40
	k=30	3965	4.01	0.85	0.27	-19.8-19.2	10.27	169	0.88	1.33	54-2033	8.54
	k=35	3965	4.09	0.85	0.22	-23.7-19.2	9.54	169	0.88	1.35	54-2033	8.51
	k=40	3965	4.02	0.85	0.26	-23.7-21.6	8.88	171	0.88	1.24	54-2033	8.63
	k=45	39	4.0	0.	0.2	-23.	8.5	17	0.	1.	37-	8.5

	65	9	85	3	7-24.0	7	1	88	22	2047	2
k=50	3965	4.12	0.85	0.21	-23.7-24.0	8.63	174	0.88	1.11	20-2047	8.58
k=60	3965	4.17	0.84	0.19	-23.7-25.0	8.56	175	0.87	1.05	20-2047	8.65
k=80	3965	4.22	0.84	0.17	-23.7-25.0	8.67	178	0.87	0.95	20-2047	8.80
k=100	3965	4.31	0.83	0.14	-23.9-25.0	8.82	182	0.86	0.84	20-2047	8.99

[1] The optimal number of analogues, and the minimum adequate number of WAPLS components

[2] The ratio of rate of change in RMSEP to rate of change in R^2

[3] The RMSEP as a percentage of the modern gradient range

The λ_1/λ_2 results of seven climatic variables for the selected calibration set (Table 3) show that MTCM, MAT, MAP, and MPWM with relatively high λ_1/λ_2 ratios can be potentially reconstructed. Pearson correlation coefficients of seven climatic variables for the selected calibration set (Table 4) indicate that there is a strong collinearity among the temperature variables (their Pearson coefficients are all greater than 0.9). Pearson coefficients for MAP vs. MAT, MAP vs. GDD5, and MAP vs. MTWM are also greater than 0.8, indicating relatively strong collinearity between MAP and MAT (GDD5 and MPWM). Combined with the results of Pearson's correlation analysis, the VIF results indicate that MTCM, MAT, and MTWM contain much co-varying information (Table 3). Firstly, one temperature variable (MTWM) and one precipitation variable (MPCM) with the lowest explanatory power are removed, the results show that the VIF values of MTCM, MAT and GDD5 still exceed 20. When GDD5 and MAT are removed in turn, there are still variables with VIF values greater than 20. Finally, only when MAT, GDD5 and MPCM are removed, the VIF values of the remaining variables are less than 20. Therefore, MTCM, MAP,

MPWM and MTWM have potentially more explanatory power for the selected calibration set.

Table 3 Summary statistics for Variance Inflation Factors (VIF), explanatory powers of 7 climatic variables as sole predictor and the ratio of the first constrained eigenvalue to the first unconstrained eigenvalue with 7 variables for the selected calibration set using canonical correspondence analysis (CCA).

Climate variables	VIF Run1	VIF Run2	VIF Run3	VIF Run4	VIF Run5	Explains % as sole predictor	λ_1/λ_2
MTCM	868.72	90.95	80.83	20.78	16.41	4.80	0.91
MAT	2685.73	169.13	79.64	-	-	4.70	0.85
MAP	22.75	8.27	8.01	7.59	8.21	4.40	0.80
MPWM	15.65	7.74	7.73	6.02	8.69	4.00	0.80
GDD5	52.84	46.97	-	22.12	-	4.50	0.77
MTWM	425.73	-	-	-	14.61	4.20	0.71
MPCM	5.56	-	-	-	-	3.30	0.54

Table 4 Pearson correlation matrix of 7 climate variables for the selected calibration set.

Pearson	MAT	MTWM	MTCM	GDD5	MAP	MPWM	MPCM
MAT	1	0.97045	0.98766	0.98485	0.80638	0.72438	0.62723
MTWM	0.97045	1	0.92199	0.97012	0.76643	0.60116	0.68485
MTCM	0.98766	0.92199	1	0.96113	0.79971	0.77228	0.57176
GDD5	0.98485	0.97012	0.96113	1	0.81653	0.70482	0.64885
MAP	0.80638	0.76643	0.79971	0.81653	1	0.8703	0.7541
MPWM	0.72438	0.60116	0.77228	0.70482	0.8703	1	0.41234
MPCM	0.62723	0.68485	0.57176	0.64885	0.7541	0.41234	1

Based on these results, MTCM is the most appropriate climate variable for the final reconstruction and MAP is also suitable. Although MAT and MTCM contain co-varying information, the MAT reconstruction may provide an additional annual perspective. Thus, MTCM, MAP and MAT are selected for the final quantitative reconstruction.

4.2. The reconstruction results

The quantitative reconstruction results of MTCM, MAP and MAT for the fossil pollen record from Lake Tengchongqinghai based on the calibration set with a 1200 km spatial extent and the WAPLS model (Fig. 3) show that MTCM and MAT change synchronously, whereas the trends of

MTCM and MAP are generally similar, except for some small differences. The climatic changes since 18.5 ka around the studied area are listed as follows:

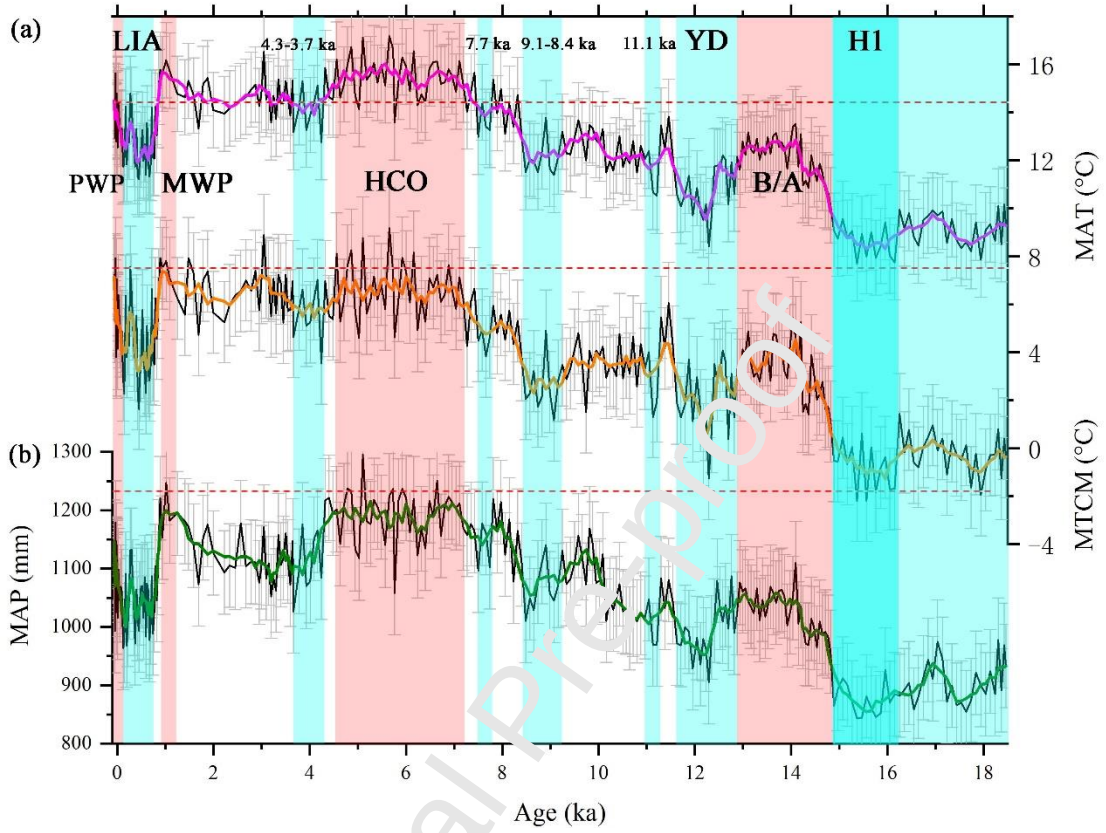

Fig. 3. Temperature and precipitation reconstructions based on the calibration set with a 1200 km spatial extent and the WAPLS model. (a) Reconstructed mean temperature of the coldest month (MTCM) and mean annual temperature (MAT) and their 5-point running means (magenta and orange thick lines). (b) Reconstructed mean annual precipitation (MAP) and its 5-point running mean (green thick line). The light-blue shadings indicate cold and dry events. The light-red shadings indicate warm and humid periods. Gray short bars indicate bootstrap sample-specific estimates of uncertainties for each reconstructed values. Red dotted lines indicate the modern observational means (1981-2010) of MAT, MTCM and MAP for Lake Tengchongqinghai.

Temperature and precipitation from 18.5-14.8 ka were the lowest since 18.5 ka, and the lowest values were concentrated between 16.2 and 14.8 ka (MTCM: averaging -0.8 °C, ranging from -2.2 to 0.6 °C; MAT: 8.6 °C, 7.7-9.6 °C; MAP: 870 mm, 840-930 mm). From 14.8 ka, temperature and precipitation increased markedly, and are in obvious high values between 14.8 and 12.8 ka (MTCM: averaging 3.3 °C, ranging from 1.1 to 5.4 °C; MAT: 12.1 °C, 10.1-13.5 °C; MAP: 1030 mm, 960-1110 mm). At 12.8 ka temperature declined significantly and the

precipitation decreased slightly with particularly low values from12.8-11.5 ka (MTCM: averaging 2.0 ℃, ranging from -1.3 to 4.1 ℃; MAT: 10.7 ℃, 8.4-12.2 ℃; MAP: 990 mm, 910-1090 mm). Between 11.5 and 7.2 ka, temperature and precipitation increased variably with three significant low intervals around 11.1 ka, 9.1-8.4 ka, and ~7.7 ka. Temperature and precipitation attained their highest values between 7.2 and 4.5 ka (MTCM: averaging 6.6 ℃, ranging from 4.6 to 9.2 ℃; MAT: 15.5 ℃, 13.6-17.1 ℃; MAP: 1190 mm,1060-1300 mm). A significant decrease in temperature occurred at 4.5 ka, whereas a significant decrease in precipitation occurred at 4.3 ka. Between 4.5 and 1.2 ka, MTCM (averaging 6.3 ℃) was only slightly lower than that during the period 7.2-4.5 ka, whereas MAT (averaging 14.6 ℃) was substantially lower. The precipitation during the period 4.3-1.6 ka (averaging 1110 mm) was markedly lower than that during the period 7.2-4.3 ka. Additionally, a low temperature and precipitation interval occurred between 4.3 and 3.7 ka (MTCM: averaging 5.5 ℃, ranging from 3.5 to 7.0 ℃; MAT: 14.0 ℃, 12.8-15.3 ℃; MAP: 1100 mm, 1030-1180 mm). Subsequently a significant warm-wet period occurred at around 1.09-0.84 ka (860-1110 CE) and the values of MTCM, MAT and MAP almost reached similar peak levels from 7.2-4.5 ka (MTCM: averaging 7.0 ℃, ranging from 6.6 to 7.9 ℃; MAT: 15.4 ℃, 15.1-16.2 ℃; MAP: 1170 mm, 1150-1250 mm). Following this warm-wet period, the coldest and driest event during the late Holocene occurred at about 0.68-0.009 ka (1270-1950 CE) (MTCM: averaging 4.2 ℃, ranging from 1.6 to 7.6 ℃; MAT: 12.7 ℃, 11.2-14.8 ℃; MAP: 1040 mm, 960-1130 mm). From 1950 CE, the temperature and precipitation increased rapidly and reached to the modern levels.

5. Discussion

5.1. Reliability of the reconstruction results

The reconstruction results are evaluated from a statistical, ecological, and climatological perspective. From statistical perspective, the plot of maximum abundance of taxa indicates that the selected modern pollen dataset covers the range of taxon abundance in the fossil samples of core TCQH1 well (Fig. 4), which reduces the possibility of no modern analogues for the fossil assemblages. This is confirmed by the goodness-of-fit analysis that shows that all fossil samples from Lake Tengchongqinghai have good or fair analogues (Fig. 5). The leave-one-out cross validation results for MTCM, MAP, and MAT of predicted (residual) vs. observed values (Fig. 6) indicate that the prediction power of WAPLS model based on the selected calibration set for MTCM and MAT is good, although there is a slight underestimate for sites with MTCM>10 °C and MAT>16 °C and a slight overestimate for sites with MTCM<-10 °C and MAT<2 °C (MTCM: RMSEP=3.35 °C, R^2=0.85; MAT: RMSEP=3.12 °C, R^2=0.81). The prediction power of MAP decreases slightly compared with that of MTCM and MAT with an underestimate for sites with MAP>1150 mm and an overestimate for MAP<600 mm (RMSEP=142 mm, R^2=0.78). This leads to some underestimation of MAP in the Middle Holocene, 1 ka, and present-day, with otherwise accurate results. The RMSEP values are smaller than the ranges of climatic variables since 18.5 ka. Furthermore, bootstrap sample-specific errors of MTCM, MAT, and MAP for each fossil sample average 0.57 °C (maximum values < 0.97 °C), 0.31 °C (maximum values < 0.54 °C), and 20 mm (maximum values < 41 mm), respectively, which are 16.9%, 10.0%, and 14.5% of the entire RMSEP values, respectively, indicating that they are reasonable (Juggins and Birks, 2012). A significance test (Telford and Birks, 2011) of the pollen-based climate reconstructions for Lake Tengchongqinghai shows that MTCM, MAT, MTWM, and GDD5 explain more variance than 95% of all the random reconstructions (Fig. 7). Although MAP fails to pass the threshold of the 95%

significance level, it passes the test of the 90% significance level (p=0.1) (Fig. S2), indicating that the MAP reconstruction may also be reliable.

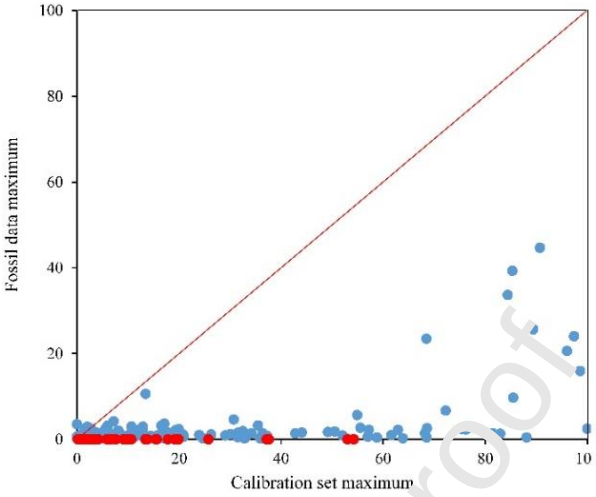

Fig. 4. Scatter plot of the maximum abundance of each taxon in the selected modern pollen dataset against that in the fossil pollen assemblage. The red circles indicate taxa in the modern pollen dataset that are not found in the fossil samples.

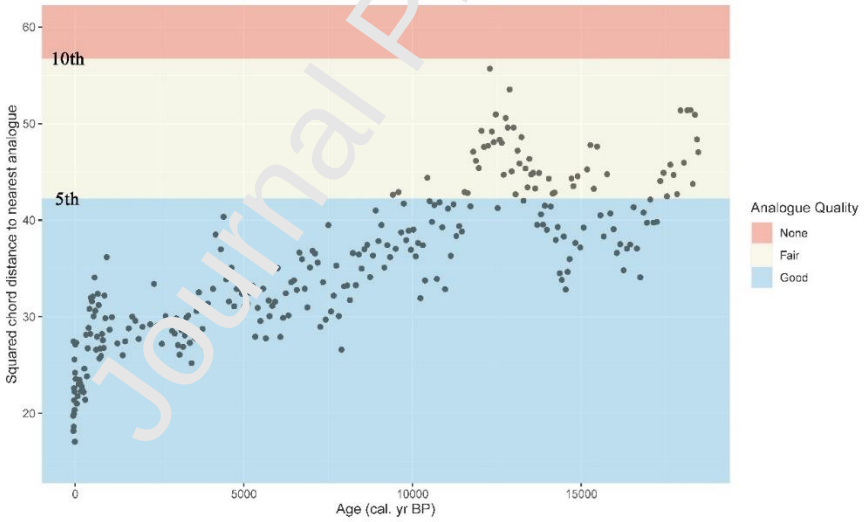

Fig. 5. Analogue quality for the reconstruction of mean temperature of the coldest month (MTCM) based on a goodness-of-fit analysis. The blue and cream shadings show the 5th and 10th percentiles of the pair-wise distribution of squared-chord distances between the fossil samples and the best analogues from the modern calibration set, respectively. Distances smaller than the 5th percentile of all distances between the calibration-set samples are considered to be good "analogues", while distances larger than the 10th percentile are considered to be "no-analogue". Distances between the 5th percentile and the 10th percentile are considered to be fair "analogues".

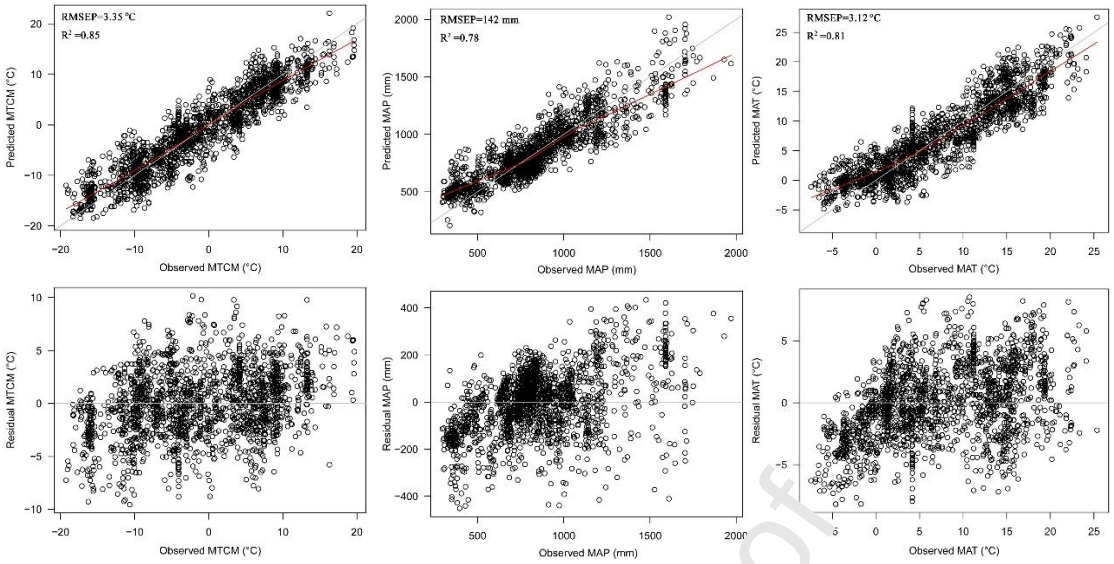

Fig. 6. Scatter plots of predicted climatic variables and residuals for WAPLS components (3 for MTCM; 2 for MAP and MAT) vs. observed values. The red lines indicate a LOWESS smoother fitted to highlight trends. The grey thin lines are 1:1 or y-axis origin lines.

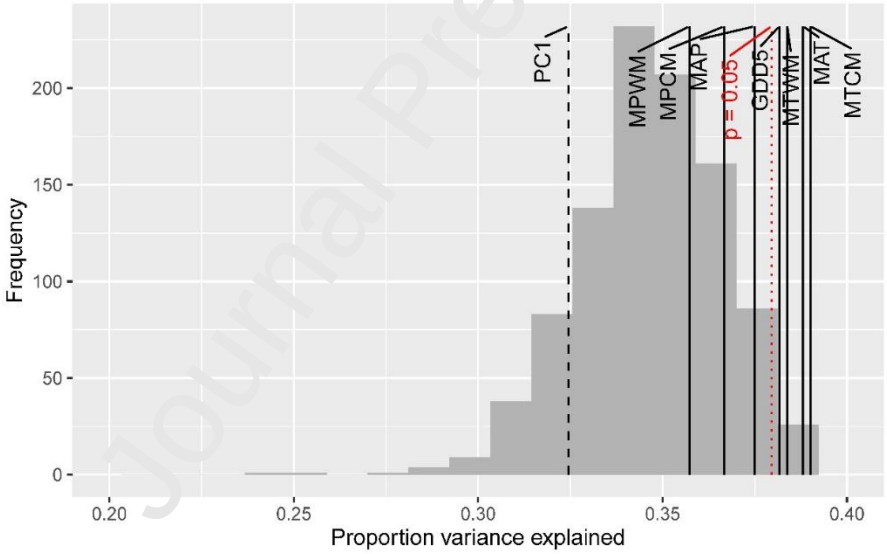

Fig. 7. Significance test results of the pollen-based climate reconstructions for Lake Tengchongqinghai. Solid black lines indicate the proportion of variance explained by different environmental variables. The red dotted line represents the test line of 95% significance level. The histogram in grey indicates the proportion of variance. The black dashed line indicates the proportion of variance explained by the first axis of a principal component analysis of the fossil pollen data. MAT: mean annual temperature, MTWM: mean temperature of the warmest month, MTCM: mean temperature of the coldest month, MAP: mean annual precipitation, MPWM: mean precipitation of the warmest month, MPCM: mean precipitation of the coldest month, GDD5: growing degree days above 5 °C.

From an ecological perspective, the quantitative reconstruction results of temperature and precipitation are roughly consistent with the qualitative reconstruction based on the fossil pollen

assemblage (Xiao et al., 2015). The WA optima and tolerance ranges for 38 major pollen taxa against MTCM, MAP and MAT (Fig. 8) show that *Myrica*, *Eurya*, *Macaranga/Mallotus*, *Castanopsis/Lithocarpus*, and *Cyclobalanopsis* have the highest WA optima for temperature (MTCM: 10.1, 9.2, 8.8, 8.2 and 7.3 °C; MAT: 16.4, 16.2, 16.3, 15.5 and 14.9 °C, respectively) and precipitation (MAP: 1260, 1200, 1210, 1320, 1140 mm, respectively), and their lowest tolerance ranges of MTCM, MAT and MAP are 2.0 °C, 9.9 °C and 860 mm, respectively. The highest pollen percentages of *Castanopsis/Lithocarpus* and *Macaranga/Mallotus*, and high *Cyclobalanopsis* percentages from 8.0-4.5 ka indicate the warmest and most humid climatic conditions since 18.5 ka. MTCM, MAT, and MAP are likely not less than 7.3 °C, 14.9 °C, and 1140 mm, respectively. Cyperaceae, Amaranthaceae/Chenopodiaceae, and *Artemisia* have very low WA optima for temperature (MTCM: -11.3, -8.9, and -6.5 °C; MAT: -0.4, 1.6, and 3.3 °C, respectively) and precipitation (MAP: 570, 520, and 620 mm, respectively) with their highest tolerance ranges of MTCM, MAT, and MAP less than 1.6 °C, 9.9 °C, and 910 mm, respectively. The highest pollen percentages of *Artemisia* and Amaranthaceae/Chenopodiaceae and relatively high Cyperaceae percentages between 18.5 and 14.8 ka suggest the coldest and driest climatic conditions, and MTCM, MAT, and MAP during this period were almost less than 1.6 °C, 9.9 °C, and 910 mm, respectively. The WA optima and tolerance ranges of *Alnus* for MTCM, MAT, and MAP are relatively high compared to other pollen types which are 3.6 (-2.1~9.2) °C, 10.8 (5.8~15.8) °C, and 940 (730~1140) mm, respectively. The highest *Alnus* pollen percentages between 4.0 and 1.0 ka indicate relatively high MTCM, MAT, and MAP which are only lower than that during the period from 7.2-4.5 ka. The WA optima and tolerance ranges for major pollen taxa against MTCM, MAP, and MAT further support the reliability of the reconstructions.

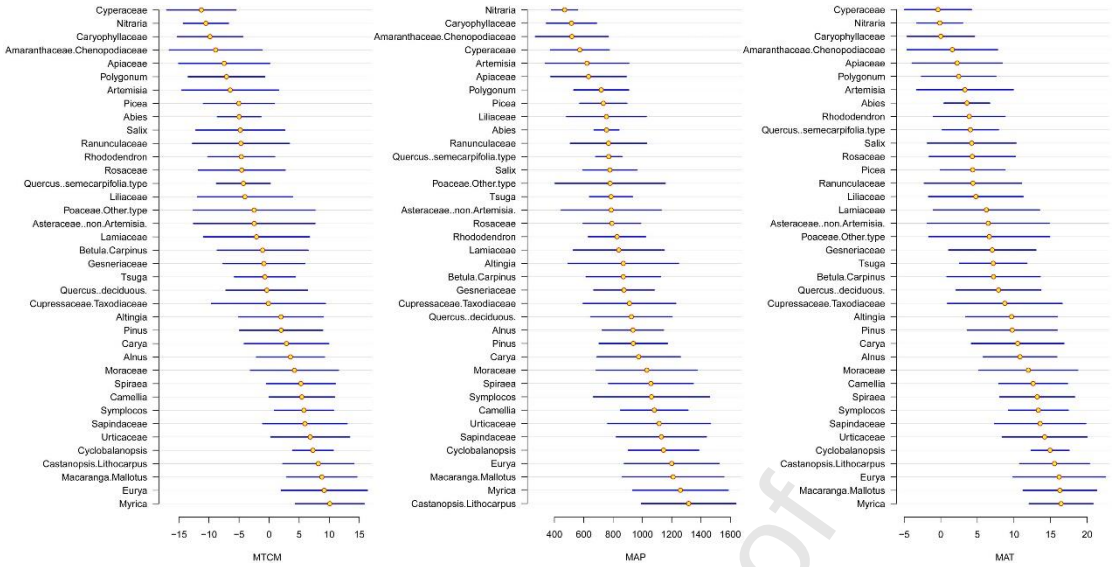

Fig. 8. Optima and tolerances of mean temperature of the coldest month (MTCM), mean annual precipitation (MAP) and mean annual temperature (MAT) for selected pollen taxa based on weighted averaging (WA) regression. The modern pollen data are from the selected calibration set. The yellow solid circles indicate the mean WA climate optima of the pollen taxa; the blue lines indicate their WA tolerances.

From a climate perspective, the pollen-based reconstructions of MTCM, MAT, and MAP for the top of the core (the mean of the upper two samples) are 7.2 °C, 14.4 °C, and 1110 mm, respectively. The quantitatively reconstructed MTCM and MAT match the Tengchong meteorological station-based values of 7.9 °C and 14.5 °C reasonably well while the quantitatively reconstructed MAP is lower than the station-based value of 1240 mm. This corresponds to the MAP model underestimation for sites >1150 mm. The total reconstructed ranges are between -2.2 and 9.2 °C for MTCM, 7.7 and 17.2 °C for MAT, and 840 and 1300 mm for MAP, which is covered by the modern climate range of pollen analogues (Fig. S3). The two brGDGT reconstructions of MAT (Fig. 9b, Tian et al., 2019; Zhao C et al., 2021) overlap with this study with similar fluctuating increases in MAT since 18.5 ka and the mid-HTM, albeit the two studies show differences from one another. The pollen-based reconstructed MAT for the top of the core in this study (14.1 °C) is closer to meteorological station-based value (14.5 °C) than that of Tian et al. (13.1 °C) and Zhao et al. (17.9 °C), indicating that our reconstructions may be more reasonable. A

recent pollen-based quantitative reconstruction spanning 68 ka from the same lake shows that the general trend of MAT since 18.5 ka is similar to this study with a temperature amplitude of 8.9 ℃ (Zhang et al., 2023). Compared with Yang et al. (2016) and Zhang et al. (2023)'s MAP reconstructions from the same lake, the overall trends and lowest values since 18.5 ka are generally similar to this study, but their fluctuation amplitudes are significantly higher. Yang et al. (2016)'s maximum MAP reached to 1660 mm at ~8.1 ka and Zhang et al. (2023)'s maximum MAP reached to 1520 mm at 8.6 ka with all values since 11.0 ka substantially higher than the modern mean of 1240 mm. This suggests that our study may underestimate MAP during wet periods, possibly due to the fewer samples with high MAP in the selected calibration set (Fig. S3). On the other hand, Yang et al. (2016) and Zhang et al. (2023) may overestimate MAP to some degree. Additionally, the reliability of all reconstructions may be influenced by human activity. Only 107 samples strongly influenced by human activity were excluded from the calibration set and the influence of human activity on the fossil pollen samples was not considered. This may be problematic in the late Holocene after 4.3 ka, and especially after 1.0 ka when the landscape was strongly influenced by human activities (Xiao et al., 2015). This is an avenue for improvement in the future work.

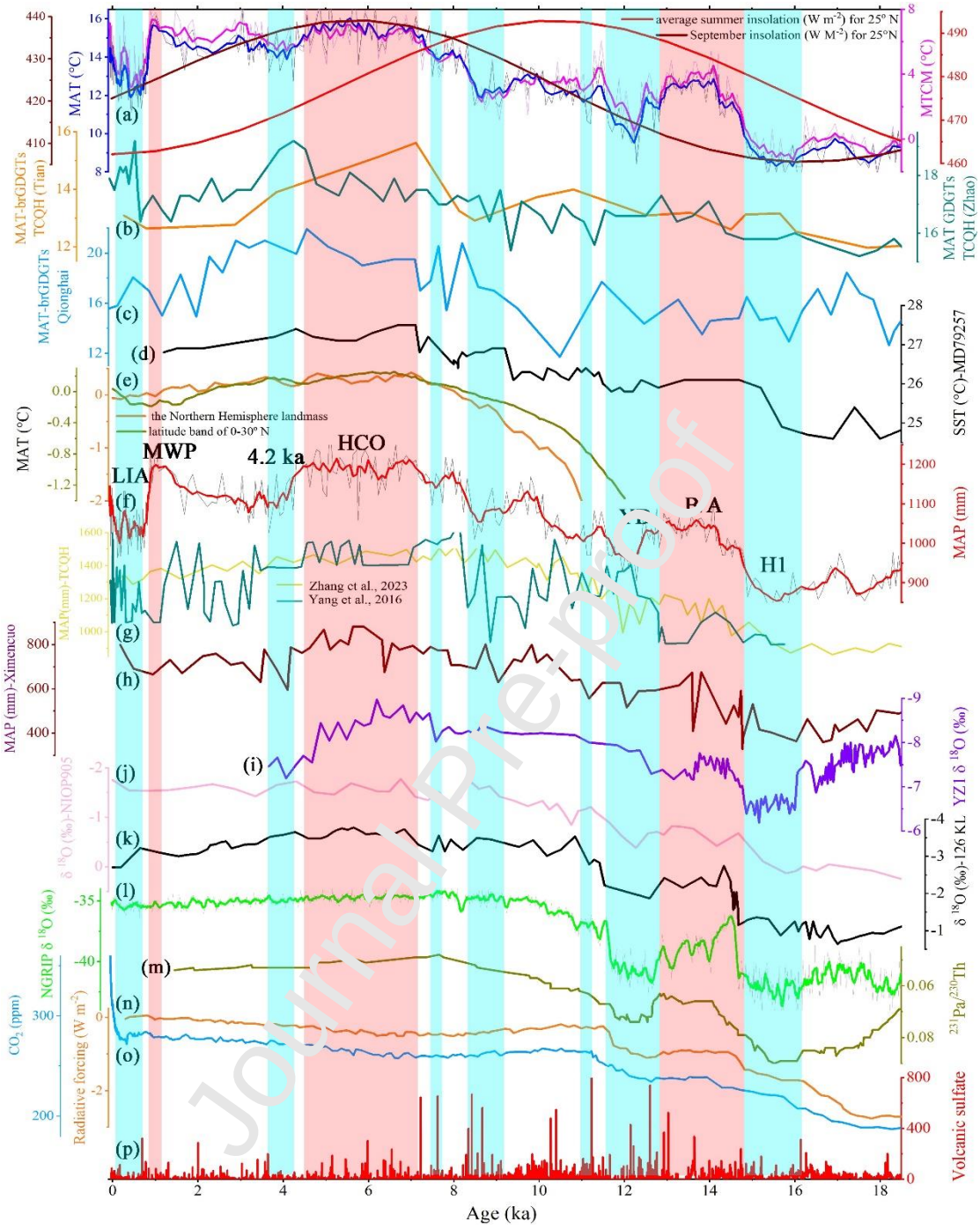

Fig. 9. Regional and global correlations and forcings since 18.5 ka. (a) Reconstructed mean temperature of the coldest month (MTCM) and mean annual temperature (MAT) and their 5-point running means (MTCM: magenta thick line; MAT: blue thick line) (this study), and average summer insolation for 25° N (red thick line) and September insolation (wine red thick line) for 25 °N (Laskar et al., 2004). (b) brGDGT-inferred MAT reconstructions from Lake Tengchongqinghai, southwestern China (orange thick line from Tian et al., 2019; deep green thick line from Zhao C et al., 2021). (c) brGDGT-inferred MAT reconstruction from Lake Qionghai, southwestern China (Wang et al., 2021). (d) SST for Core MD79257, the southern Indian Ocean (Sonzogni et al., 1998). (e) Reconstructed MATs for the latitude band of 0-30° N (deep yellow thick line, Kaufman et al., 2020) and the NH landmass (orange thick line, Zhang W et al., 2022). (f) Reconstructed mean annual precipitation (MAP)

and its 5-point running mean (this study). (g) Pollen-based MAP reconstructions from Lake Tengchongqinghai, southwestern China (deep cyan thick line from Yang et al., 2016; mimosa yellow thick line from Zhang et al., 2023). (h) Pollen-based MAP reconstruction from Lake Ximencuo, the eastern Tibetan Plateau (Herzschuh et al., 2014). (i) The YZ1 stalagmite $\delta^{18}O$ record, southwestern China (Wu et al., 2020). (j) The $\delta^{18}O$ record of the planktic foraminifera *G. rubber* for core NOIP905, western Arabian Sea (Huguet et al., 2006). (k) The $\delta^{18}O$ record of the planktic foraminifera *G. rubber* for core KL 126 in the Bay of Bengal (Kudrass et al., 2001). (l) The $\delta^{18}O$ record from the NGRIP ice-core record (Lowe et al., 2008). (m) The $^{231}Pa/^{230}Th$ composite curve (9-point moving average) (Ng et al., 2018). (n) The combined radiative forcing from CO_2, CH_4, and N_2O relative to preindustrial levels (Clark et al., 2012; Marcott et al., 2013). (o) Atmospheric CO_2 concentrations from the Law Dome ice core (MacFarling Meure, et al., 2006) and EPICA Dome C ice core (Monnin et al., 2001). (p) The volcanic sulfate record in the GISP2 core (Zielinski et al., 1997). The light-blue shadings indicate cold and dry events. The light-red shadings indicate warm and humid periods.

5.2. Comparisons with regional or over-regional climatic reconstructions

The synchronous changes of MTCM, MAT, MTWM, and GDD5 (Fig. S4) in this study suggest that there are no obvious seasonal biases in temperature since the last deglaciation. This conclusion undermines the interpretation of seasonal biases in proxies as the main origin of model–data discrepancies (Liu et al., 2014; Bova et al., 2021). Additionally, temperature and precipitation are not decoupled even during the early Holocene (Fig. 3), which is different from pervious conclusions (Wu et al., 2013). Our results reveal that temperature and precipitation increased variably from 18.5 ka and peaked from 7.2-4.5 ka when MAT was on average 1.0 ℃ higher than the modern observation value and MTCM and MAP were often higher than the modern observation values; these values then decreased gradually (Fig. 3, 9a, f). This pattern of the warmest and wettest conditions in the middle Holocene is different from the prevailing view of an early Holocene or early to middle Holocene ISM maximum (Gupta et al, 2003; Dykoski et al., 2005; Fuchs and Buerkert, 2008; Rao et al., 2016), but it exists commonly in other records in southwestern China and other regions affected by the ISM. For example, brGDGT MAT reconstructions from Lake Tengchongqinghai (Fig. 9b, Tian et al., 2019; Zhao C et al., 2021), Lake Qionghai (Fig. 9c, Wang et al., 2021), and Hongyuan Peatland (Yan et al., 2021) in

southwestern China show this pattern. Zhang et al. (2017) suggested a generally warmer period between ~8.5 and ~6.0 ka based on subfossil chironomids from Lake Tiancai, southwestern China. The pollen record from Lake Tianchi in southwestern China revealed maximum monsoonal precipitation between 7.1–6.4 ka, coinciding with peak Holocene warmth (Jiang et al., 2019). Slightly further afield, SSTs based on the unsaturation index of C_{37} alkenone from core MD79257, the southern Indian Ocean, suggested Holocene maximum SSTs at 7-6 ka (Fig. 9d, Sonzogni et al., 1998). A pollen-based MAP reconstruction from Lake Ximencuo, the eastern TP (Fig. 9h, Herzschuh et al., 2014), a pollen record from Lake Tiancai in northwestern province (Xiao et al., 2014a), the YZ1 stalagmite $\delta^{18}O$ record in southwestern China (Fig. 9i, Wu et al., 2020), sediment total reflectance from the northeastern Arabian Sea (Deplazes et al., 2013), and $\delta^{18}O$ records of the planktic foraminifera *Globigerinoides ruber* for core NOIP905 in western Arabian Sea (Fig. 9j, Huguet et al., 2006) and for core KL 126 in the Bay of Bengal (Fig. 9k, Kudrass et al., 2001) all suggested a mid-HTM. Considering these and other studies (Yi et al., 2003; Liew et al., 2006; Liu et al., 2015; Rao et al., 2016), we support Jiang et al. (2019)'s interpretation of synchronous changes in the ISM and the EASM since the last deglaciation.

In addition, hemispheric and global-scale temperature reconstructions revealed similar results. Reconstructed NH annual, summer, and winter temperatures based on 1310 pollen records are all characterized by a rapid warming from the early to middle Holocene (11–7 ka) and gradual cooling after ~7 ka (Fig. 9e, orange thick line, Zhang W et al., 2022). Multi-method median global mean surface temperature reconstruction and MAT reconstruction for the latitude band of 0-30° N (Fig. 9e, deep yellow thick line, Kaufman et al., 2020) from the Temperature 12k database show that peak warmth was centered on about 6.5 ka. Recently, simulation results based on time slices

of the Community Earth System Model show that vegetation-induced warming gave rise to a mid-HTM at 6 ka, followed by a cooling trend toward the preindustrial era (PI) (Thompson et al., 2022). This is consistent with our pollen-based reconstructions but contrasts with traditional simulations of long-term warming through the Holocene. Thompson et al. (2022) highlighted the role of NH vegetation change in driving a mid-HTM, providing a potential explanation for this discrepancy.

Under the background of this trend, our quantitative reconstruction results revealed seven abrupt cold and dry events occurring at 16.2-14.8 ka, 12.8-11.5 ka, ~11.1 ka, 9.1-8.4 ka, ~7.7 ka, 4.3-3.7 ka and 0.68-0.009 ka (1270-1950 CE), respectively. The cold and dry events during the periods of 16.2-14.8 ka, 12.8-11.5 ka, 4.3-3.7 ka, and 0.68-0.009 ka (1270-1950 CE) correspond to H1, the YD, the 4.2 ka event, and the LIA, respectively. During H1, MTCM, MAT, and MAP average 8.7 °C, 5.9 °C, and 370 mm drops relative to the modern observational values, respectively; during the YD, 5.9 °C, 3.8 °C, and 250 mm drops; for the 4.2 ka event, 2.7 °C, 0.5 °C, and 130 mm drops; for the LIA, 3.7 °C, 1.8 °C, and 200 mm drops. Between the H1 and the YD, there is a warm and humid period (14.8-12.8 ka) corresponding to the Bølling/Allerød warm period (B/A), when MTCM, MAT, and MAP average 4.6 °C, 2.4 °C, and 210 mm lower than the modern observational values. Before the LIA, a warm and humid period from 1.09-0.84 ka (860-1110 CE) corresponds to the Medieval Warm Period (MWP). Lastly, the rapid increases in the temperature and precipitation from 1950 CE match the Present Warm Period (PWP). Other high-resolution studies from southwestern China showed that the H1, the BA, and the YD during the last deglaciation were ubiquitous (Dykoski et al., 2005; Herzschuh et al., 2014; Xiao et al., 2014b, 2015; Zhang et al., 2019; Wu et al., 2020). These abrupt events are also common in other

records from the ISM region, such as SSTs for core MD79257 in the southern Indian Ocean (Fig. 9d, Sonzogni et al., 1998), sediment total reflectance from the northeastern Arabian Sea (Deplazes et al., 2013), $\delta^{18}O$ records from the planktic foraminifer *G. ruber* from core NIOP905 in the western Arabian Sea (Fig. 9j) (Huguet et al., 2006) and core KL126 in the Bay of Bengal (Fig. 9k) (Kudrass et al., 2001), as well as the EASM region (Wang et al., 2001; Chen et al., 2015; Yang et al., 2018), the North Atlantic (Duplessy et al.,1992; Waelbroeck et al., 2001; Yasuhara et al., 2019), and the Greenland ice core (Grootes and Stuiver, 1997; Lowe et al., 2008, Fig. 9l).

The three cold-dry events that occurred in the early and middle Holocene (at 11.1 ka, 9.1-8.4 ka, and ~7.7 ka) are not universal as H1, the B/A, and the YD, but are inferred at sites around the world. For example, the 11.1 ka cold-dry event corresponds to a weak ISM interval recorded in $\delta^{13}C$ values from the Hongyuan peat bog on the TP (Hong et al., 2003), and *G. bulloides* percentage in hole 723A from the northwestern Arabian Sea (Gupta et al., 2005), a subalpine pollen sequence in Taiwan (Liew et al. 2006), and abrupt ocean surface cooling characterized by the ice-rafted debris in the North Atlantic (Bond et al., 1997). The cold and dry event from 9.1-8.4 ka matches well with the cold event between 8.7 and 8.3 ka found on the central TP (Herzschuh et al., 2006), the weak ISM interval from 9.5-8.6 ka in hole 723A from the northwestern Arabian Sea (Gupta et al., 2005), the weak EASM event at ~9.5–8.5 ka (Chen et al., 2015), and the pronounced cooling period between 8.9 and 8.3 ka reconstructed from Deep Lake in Minnesota, USA (Hu et al., 1999). Moreover, Mayewski et al. (2004) revealed a significant rapid climate change from 9-8 ka characterized by high-latitude cooling and low-latitude aridity. The ~7.7 ka cold-dry event was also detected on the central (Herzschuh et al., 2006) and western (Gasse, 1996) TP, in hole 723A from the northwestern Arabian Sea (Gupta et al., 2005), a

subalpine pollen sequence in Taiwan (Liew et al. 2006), and a deep-sea sediment core off South Australia (Moros et al., 2009). The 4.2 ka event is considered to have been a relatively sustained and widespread phenomenon throughout the low- and mid-latitude regions in the NH (Bond et al., 1997; Johnsen et al., 1997; Thompson et al., 2002; Booth et al., 2005; Nakamura et al., 2016). It was widely reported in the ISM region (Hong et al., 2003; Gupta et al., 2005; Moros et al., 2009; Herzschuh et al., 2014; Nakamura et al., 2016; Wu et al., 2020, Fig. 9i) and the EASM region (Wang et al., 2005; Xiao et al., 2018; Cai et al., 2021; Wang et al. 2022), where it is characterized by weak summer monsoon. The significant warm-humid MWP and cold-dry LIA detected in this study also exist in most paleoclimate studies of the last 2,000 years around the world (Soon et al., 2003). A warmer and more humid MWP than PWP are similar to results of other published studies (Soon et al., 2003; Ge et al., 2013). Ge et al. (2013) has suggested that all temperature sequences indicate warm conditions from 985-1140 CE and after 1945 CE with cold conditions between 1440 and 1880 CE. Most sequences indicate warm conditions from 841 to 1290 CE, cold conditions between 1291 and 1910 CE, and warming again after 1910 CE (Ge et al., 2013). These warm and cold phases are temporally very consistent with the start and end times of MWP, LIA and PWP in this study.

5.3. Possible dynamic mechanisms

Comparing the quantitative reconstructed climatic sequences with climate forcings (Fig. 9), it can be seen that the general increasing trends in temperature and precipitation from 18.5 ka may be driven by the increase of summer (June, July, August) insolation at 25 ºN from ~20 ka (red line in Fig. 9a) (Laskar et al., 2004) and strengthened by the increases of the radiative forcing (Fig. 9n) (Clark et al., 2012; Marcott et al., 2013) and asmospheric CO_2 concentrations (Fig. 9o) (Monnin et

al., 2001; MacFarling Meure et al., 2006) from ~17.5 ka. Temperature and precipitation culminated from 7.2-4.5 ka, which lagged peak summer insolation values by about 3000 years. To explain this lag, changes in glacial boundary conditions (e.g., ice volume, SST, albedo, and atmospheric trace-gas concentrations) have been cited as mechanisms that can alter the way in which the climate responds to summer insolation (deMenocal and Rind, 1993; Overpeck et al., 1996; Griffiths et al., 2009). For example, the highest SSTs at ~7.0 ka documented in the western Arabian Sea (Naidu and Malmgren, 2005) and a plateau in sea-level rise at ~6.5 ka inferred from $\delta^{18}O$ values of Red Sea benthic foraminifera (Siddall et al., 2003) and Barbados coral reefs from the eastern Caribbean Sea (Peltier and Fairbanks, 2006) are very important regional forcing mechanisms for the mid-HTM in the ISM region (Xiao et al., 2014a, 2015). After 4.5 ka, the general declining trends in temperature and precipitation are in concert with slowly decreasing summer insolation. Additionally, temperature and precipitation trends match September solar insolation for 25°N (brown line in Fig. 9a), suggesting a possibly important factor for the study area (Xiao et al., 2015).

The abrupt cold events during the last deglaciation (H1 and the YD) correspond well to the slowdown of the Atlantic meridional overturning circulation (AMOC) as indicated by the $^{231}Pa/^{230}Th$ proxy in sediment cores from the west and deep high-latitude North Atlantic (Fig. 9m) (Ng et al., 2018). Changes in AMOC directly affected North Atlantic climate, and in turn affected the monsoon and the mean latitudinal position of the Intertropical Convergence Zone (ITCZ) (Wang et al., 2007). This climate pattern was additionally facilitated by a slowdown of the rate of increased radiative forcing (Fig. 9n) and atmospheric CO_2 concentrations (Fig. 9o) from 16.2-14.8 ka and the decreases in the radiative forcing (Fig. 9n) and CO_2 concentrations (Fig. 9o) from

12.8-11.5 ka which was also accompanied by elevated values of volcanic sulfates (Fig. 9p) (Zielinski and Mershon, 1997). AMOC (Alley et al., 1997; Barber et al., 1999) and solar forcing have been put forward to explain early Holocene climate instability (Herzschuh et al., 2006). However, the three cold-dry events at 11.1 ka, 9.1-8.4 ka, and ~7.7 ka correspond well to the increased values of volcanic sulfates (Fig. 9p), indicating the important role of volcanic eruptions. At about 4.2 ka, summer insolation reached its lowest level and September solar insolation also decreased significantly, which resulted in a southward retreat of the ITCZ (Fleitmann et al., 2007). Relatively low total solar irradiance (TSI) inferred from ^{10}Be in polar ice cores and ^{14}C in tree rings (Steinhilber et al., 2012) from 4.5-4.0 ka and a negative phase of the Indian Ocean Dipole at 4.2 ka (Berkelhammer et al., 2012; Nakamura et al., 2016) also contributed to the widespread 4.2 ka event. Based on the simulation results with all forcings, individual forcings, natural factor combinations, and human factor combinations (Ge et al., 2015), climate during the MWP and LIA was mainly controlled by changes in solar activity. This is supported by the high values from 1.22-0.68 ka (730-1270 CE) and low values between 1270 and 1920 CE of TSI (Steinhilber et al., 2012). The cause of warming during the PWP is clearly different than the MWP and is mainly controlled by the rapid increase of greenhouse gases (such as CO_2) (Fig. 9o, MacFarling Meure et al., 2006) (Ge et al., 2015).

A cross-correlation analysis between a final monotonic trend (IMF6: intrinsic mode functions) decomposed from the MAT through ICEEMDAN (Fig. S5) and average summer insolation (or September solar insolation) was conducted for this study. The results (Fig. 10) showed that the highest correlation values (mean of 0.97) between MAT and average summer insolation occurred at positive lags with ~70 samples, indicating that average summer insolation led MAT by ~5 ka.

The highest correlation values (mean of 0.96) between MAT and September solar insolation occurred at positive lags with several samples, indicating that September solar insolation only led MAT by several hundred years. These high correlation values and positive lags are strong evidence of driving forces. The modulation role of greenhouse gas concentrations and radiative forcing can be revealed with wavelet coherences (Fig. 11). The time series of IMF4 and IMF5 decomposed from the MAT through ICEEMDAN (Fig. S5) and climate forcings with trends removed shows an in-phase relationship between CO_2 (or radiative forcing) and MAT in the area of a time frequency plot above the 5% significance level, with CO_2 (or radiative forcing) leading MAT.

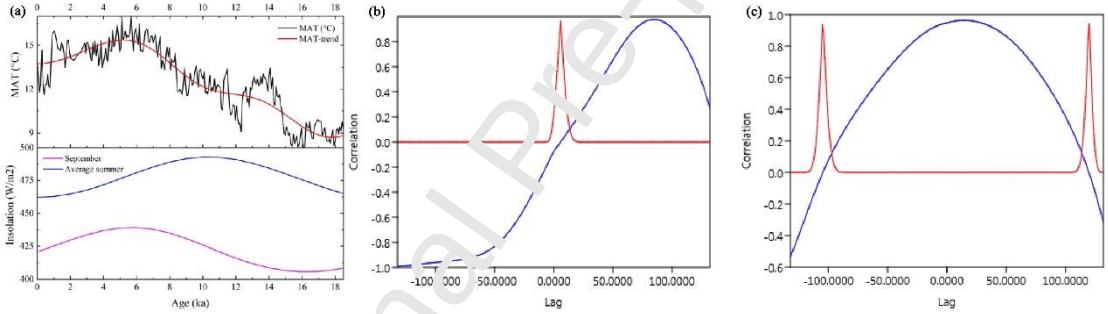

Fig. 10 Cross correlation between the trend of the reconstructed MAT and average summer insolation (or September insolation). (a) Time series plots for the reconstructed MAT and the trend of MAT, average summer insolation, and September insolation. (b) Cross correlation between the trend of MAT and average summer insolation. (c) Cross correlation between the trend of MAT and September insolation. Blue curve indicates the cross-correlation value at each lag time. Red curve indicates p values drawing the significance of the correlation. Each lag is 70 years.

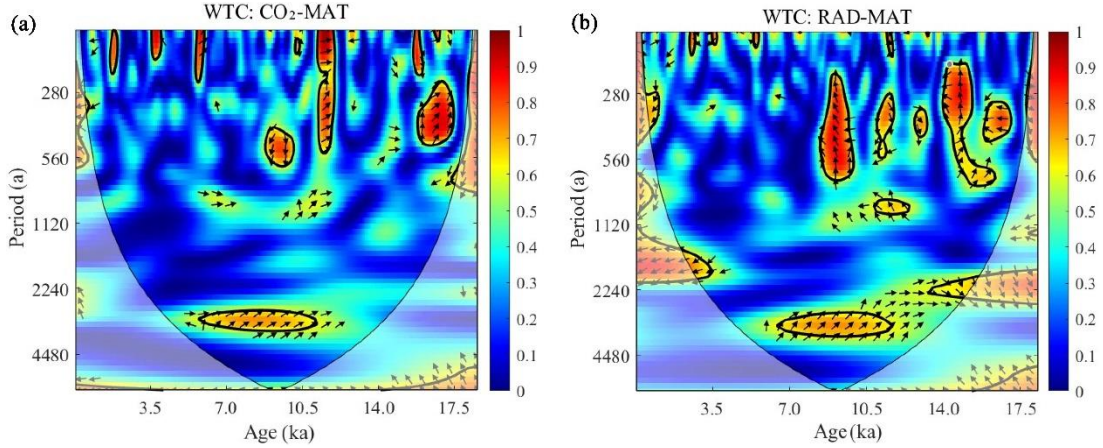

Fig. 11 Wavelet coherences between climate forcings (the CO_2 concentration and the radiative forcing) removing the trends and the reconstructed MAT time series (IMF4+5). The 5% significance level against red noise is shown as a thick contour. The relative phase relationship is shown as arrows (with in-phase pointing right, anti-phase pointing left, and climate forcings leading the reconstructed MAT by 90° pointing straight up).

Spectral analysis can aid in delineating the factors that force the monsoon by looking at the cyclicity of climatic proxies. In this study, MTCM, MAT, and MAP were selected to carry out REDFIT spectral analysis (Figure 12). All exhibit the strongest 4650-year cycle above the 99% chi2 red-noise level and significant cycles of 250, 180, 160, and 130 years above the 90% chi2 red-noise level. Spectral analysis of MTCM also reveals significant cycles of 530, 300, and 200 years above the 90% chi2 red-noise level, and MAP has significant cycles of 190 and 150 years above the 90% chi2 red-noise level.

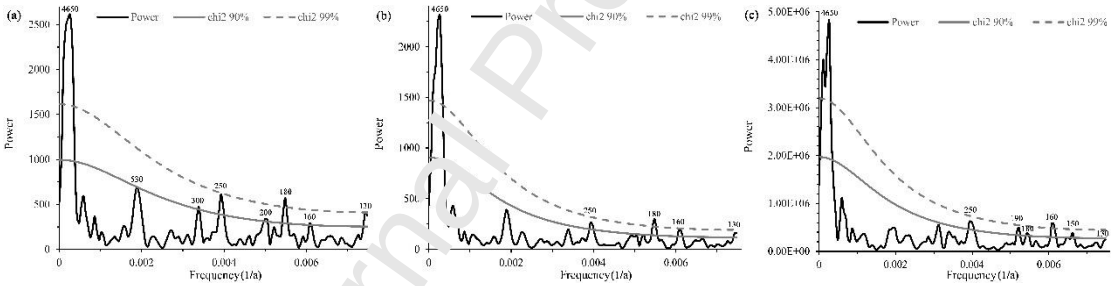

Fig. 12. Spectral analysis of MTCM (a), MAT (b) and MAP (c). The spectral analysis was done using REDFIT spectral analysis in PAST software version 4.11 (Hammer et al., 2001). The utilized parameters were: window: welch; oversample: 2; segments: 3. The gray dash and solid lines represent the 99% and 90% of the chi-squared confidence level, respectively.

The strongest 4650-year cycle matches well the 4670-year periodicity revealed in the ice-rafted debris records in the North Atlantic (Bond et al., 1997; Keeling and Whorf, 2000). Similar cycles were also found in the *Tsuga* pollen percentage time series from Lake Chenghai, southwestern China (at 4163 year) (Xiao et al., 2018), Arabian Sea upwelling (at 4400 year) (Leuschner and Sirocko, 2003), percent carbonate data from the western subtropical North Atlantic (at 4500 year) (Keigwin and Jones, 1994), carbonate time series from site 1061 in the

western North Atlantic (at 4000 year) (Grützner et al., 2002), the polar and low- to mid-latitude circulation index in the NH (at 4500 year) (Mayewski et al., 1997), $\delta^{18}O$ of diatom from Lake Malawi in Africa (at 4500 year) (Barker et al., 2007), and Vostok temperatures in Antarctica (at 4400 year) (Yiou et al., 1991, 1995). All these indicate that the ~5000-year cycle is ubiquitous around the world. A combination of precessional and obliquity frequencies have been proposed as mechanisms behind this cycle (Pestiaux et al., 1988; Yiou et al., 1991, 1995).

The cycles of 530, 300, 250, 200, 190, 180, 160, 150, and 130 years documented in this study are close to significant centennial cycles of 558, 206, and 159 years in the stalagmite $\delta^{18}O$ record from Dongge Cave, southern China (Wang et al., 2005) and 470, 320, 220, 156, and 126 years in sediments of the Arabian Sea (Thamban et al., 2007). Most of these cycles match closely with significant cycles of 512, 206, and 148 years in the $\Delta^{14}C$ record (Stuiver and Braziunas, 1993) and sunspot numbers (226, 209, 150, 132 years) (Gupta et al., 2005), indicating a century-scale relationship between solar changes and the ISM. In addition, the ~500-year cycle has been reported in many records in the ISM (Bhushan et al., 2001; Thamban et al., 2007; Kessarkar et al., 2013; Gayathri et al., 2022) and EASM regions (Xu et al., 2014), the GISP2 $\delta^{18}O$ record (Stuiver et al., 1995), and North Atlantic Deep Water (NADW) circulation (Chapman and Shackleton, 2000). All these imply that this cycle is widespread in the NH, which may be related to the AMOC control on incorporation of the ^{14}C into the ocean (Stuiver and Braziunas, 1993; Chapman and Shackleton, 2000; Neff et al., 2001). In the ISM region, the ~500-year cycle was attributed to the modulation of monsoon by NADW formation (Bhushan et al., 2001). Considering the ITCZ connection of the ISM with the EASM, this cycle of 500 years could be also related to the position of the ITCZ (Kessarkar et al., 2013). The ~200-yr Suess solar cycle (Suess, 1980; Usoskin and

Mursula, 2003) is widely ascribed to be of solar origin (Stuiver and Braziunas, 1989, 1993; Stuiver et al., 1995; Agnihotri et al., 2002; Thamban et al., 2007), and has been noted in many paleoclimate records from the ISM region (Neff et al., 2001; Agnihotri et al., 2002; Berger and von Rad, 2002; Staubwasser et al., 2002; Fleitmann et al., 2003; Tiwari et al., 2005; Gayathri et al., 2022). This century-scale relationship between solar activity and ISM variability reinforces the hypothesis that the intensity of Asian monsoon is affected by variations in solar activity (Kerr, 2005; Tiwari et al., 2005; Wang et al., 2005).

6. Conclusions

Based on an updated modern pollen dataset comprising 4258 samples and a high-resolution pollen record spanning the last 18.5 ka from Lake Dongchongqinghai in southwestern China, this study quantitatively reconstructed several climate variables. This was performed by screening modern pollen data, selecting an appropriate calibration set, analyzing the major climate factors, selecting an appropriate model, and assessing the reconstruction results from using statistical, ecological, and climatic perspectives. The following conclusions are drawn:

(1) MAP was the main controlling factor for the calibration sets with radii of the modern sites around the core site larger than 1300 km. MTCM was the main controlling factor for the calibration sets with radii between 1300 and 1000 km and GDD5 was the main controlling factor for sets with radius less than 1000 km.

(2) The WAPLS model and the calibration set with the modern sites within a radius of 1200 km around the core site were selected as the most reliable model and most appropriate calibration set for final quantitative reconstructions of MTCM, MAT, and MAP.

(3) The quantitative reconstructions show that the temperature and precipitation in the study

area increased variably but gradually from 18.5 ka, and peaked from 7.2-4.5 ka when MAT was on average 1.0 °C higher than the modern observational value (14.5 °C), corresponding to the mid-HTM, and then decreased gradually. Additionally, seven abrupt cold and dry events were identified from 16.2-14.8 ka, 12.8-11.5 ka, 4.3-3.7 ka, and 0.68-0.009 ka (1270-1950 CE) which corresponded to H1, the YD, the 4.2 ka event, and the LIA, respectively. The other three, less common cold-dry events occurred at ~11.1 ka, 9.1-8.4 ka, and ~7.7 ka.

(4) Using cross-correlation, spectral, and wavelet analysis, we conclude that the climate trends since 18.5 ka in this study area were primarily driven by summer and September solar insolation, and changes in radiative forcing and greenhouse gas concentrations also played an important modulation role. Abrupt changes may be caused by AMOC, solar activity, the position of the ITCZ, and volcanic activity.

Declaration of competing interest

The authors declare they have no conflict of interest.

Acknowledgements

This work was financially supported by the National Key Research and Development Program of China (grant number 2016YFA0600501), the National Natural Science Foundation of China (grant numbers 41877434, 42077424, 42277446). Xiangjie Chen was thanked for her assistance with single pollen grain technique and partially SEM examination (supported by grant number 41877437).

References

Agnihotri, R., Dutta, K., Bhushan, R., Somayajulu, B.L.K., 2002. Evidence for solar forcing on the Indian monsoon during the last millennium. Earth Planet. Sc. Lett. 198, 521-527.

Alley, R.B., Clark, P.U., 1999. The deglaciation of the northern hemisphere: a global perspective. Annu. Rev. Earth Pl. Sc. 27, 149-182.

Alley, R.B., Mayewski, P.A., Sowers, T., Stuiver, M., Taylor, K.C., Clark, P.U., 1997. Holocene climate instability: a prominent widespread event 8200 yr ago. Geology 25, 483–486.

Barber, D.C., Dyke, A., Hillaire-Marcel, C., Jennings, A.E., Andrews, J.T., Kerwin, M.W., Bilodeau, G., McNeely, R., Southon, J., Morehead, M.D., Gagnon, J.-M., 1999. Forcing of the cold event of 8200 years ago by catastrophic drainage of Laurentide lakes. Nature 400, 344–348.

Barker P.A., Leng M.J., Gasse F., Huang Y., 2007. Century to-millennial scale climatic variability in Lake Malawi revealed by isotope records. Earth Planet. Sc. Lett. 261, 93–103.

Benn D.I., Owen, L.A.,1998. The role of the Indian summer monsoon and the mid-latitude westerlies in Himalayan glaciation: Review and speculative discussion. J. Geol. Soc. London. 155, 353–363.

Berger, W.H., von Rad, U., 2002. Decadal to millennial cyclicity in varves and turbidites from the Arabian Sea: hypothesis of tidal origin. Global Planet. Change, 34, 313–325.

Berkelhammer, M., Sinha, A., Stott, L., Cheng, H., Pausata, F.S.R., Yoshimura, K., 2012. An abrupt shift in the Indian monsoon 4000 years ago. American Geophysical Union Geophysical Monograph 198, 75-87.

Bhushan, R., Dutta, K., Somayajulu, B.L.K., 2001. Concentrations and burial fluxes of organic and inorganic carbon on the eastern margins of the Arabian Sea. Mar. Geol. 178, 95–113.

Birks, H.J.B., 2012. Overview of numerical methods in palaeolimnology, in: Birks, H.J.B., Lotter, A.F., Juggins, S., Smol, J.P. (Eds.), Tracking Environmental Change Using Lake Sediments Vol. 5: Data Handling and

Numerical Techniques. Springer Dordrecht, Dordrecht, pp. 19–92.

Birks, H.J.B., Heiri, O., Seppä, H., Bjune, A.E., 2010. Strengths and weaknesses of quantitative climate reconstructions based on late-quaternary biological proxies. Open Ecol. J. 3, 68–110.

Bond G, Showers W, Cheseby M., Lotti, R., Almasi, P., 1997. A Pervasive Millennial-Scale Cycle in North Atlantic Holocene and Glacial Climates. Science 278, 1257-1266.

Booth, R.K., Jackson, S.T., Forman, S.L., Kutzbach, J.E., Bettis, E.A., Kreig, J., Wright, D. K., 2005. A severe centennial-scale drought in mid-continental North America 4200 years ago and apparent global linkages. Holocene 15, 321-328.

Bova, S., Rosenthal,Y., Liu, Z., Godad,S.P., Yan, M., 2021. Seasonal origin of the thermal maxima at the Holocene and the last interglacial. Nature 589, 548-553.

Cai, Y.J., Cheng, X., Ma, L., Mao, R.X., Breitenbach, S.F.M., Zhang, H.W., Xue, G., Cheng, H., Edwards, R.L., An, Z.S., 2021. Holocene variability of East Asian summer monsoon as viewed from the speleothem $\delta^{18}O$ reconrds in central China. Earth Planet. Sc. Lett. 558, 116758.

Cao, X., Tian, F., Telford, R.J., Ni, J., Xu, Q., Chen, F., Liu, X., Stebich, M., Zhao, Y., Herzschuh, U., 2017. Impacts of the spatial extent of pollen-climate calibration-set on the absolute values, range and trends of reconstructed Holocene precipitation. Quat. Sci. Rev. 178, 37-53.

Chapman, M.R., Shackleton, N.J., 2000. Evidence of 550-year and 1000-year cyclicities in North Atlantic circulation patterns during the Holocene. Holocene 10, 287-291.

Chen, F.H., Xu, Q.H., Chen, J.H., Birks, H.J.B., Liu, J.B., Zhang, S.R., An, C.B., Telford, R.J., Cao, X.Y., Wang, Z.L., Zhang, X.J., Selvaraj, K., Lu, H.Y., Li, Y.C., Zheng, Z., Wang, H.P., Zhou, A.F., Dong, G.H., Zhang, J.W., Huang, X.Z., Bloemendal, J., Rao, Z.G., 2015. East Asian summer monsoon precipitation variability since the last deglaciation. Sci. Rep. 5, 11186.

Chevalier, M., Davis, B.A.S., Heiri, O., Seppä, H., Chase, B.M., Gajewski, K., Lacourse, T., Telford, R.J., Finsinger, W., Guiot, J., Kühl, N., Maezumi, S.Y., Tipton, J.R., Carter, V.A., Brussel, T., Phelps, L.N., Dawson, A., Zanon, M., Vallé, F., Nolan, C., Mauri, A., de Vernal, A., Izumi, K., Holmström, L., Marsicek, J., Goring, S., Sommer, P.S., Chaput, M., Kupriyanov, D., 2020. Pollen-based climate reconstruction techniques for late Quaternary studies. Earth Sci. Rev. 210, 103384.

Clark, P.U., Shakun, J.D., Baker, P.A., Bartlein, P.J., Brewer, S., Brook, E., Carlson, A.E., Cheng,H., Kaufman, D.S., Liu, Z.Y.,Marchitto, T.M., Mix, A.C., Morrill, C., Otto-Bliesner, B.L., Pahnke, K., Russell, J.M., Whitlock, C., Adkins, J.F., Blois, J.L., Clark, J., Colman, S.M., Curry, W.B., Flower, B.P., He, F., Johnson, T.C., Lynch-Stieglitz, J., Markgraf, V., McManus, J., Mitrovica, J.X., Moreno, P.I., Williams, J.W., 2012. Global climate evolution during the last deglaciation. P. Natl. Acad. Sci. USA, 109, E1134–E1142.

Colominas M.A., Schlotthauer G., Torres M. E., 2014. Improved Complete Ensemble EMD: a suitable tool for biomedical signal processing. Biomed. Signal Proces. 14, 19–29.

Compiling Group of Yunnan Vegetation. Vegetation of Yunnan. Beijing: Science Press, 1987. 417, 771-773 (in Chinese).

Davis, B.A.S., Brewer, S., Stevenson, A.C., Guiot, J., 2003. The temperature of Europe during the Holocene reconstructed from pollen data. Quat. Sci. Rev. 22, 1701-1716.

deMenocal, P.B., Rind, D., 1993. Sensitivity of Asian and African climate to variations in seasonal insolation, glacial ice cover, sea surface temperature, and Asian orography. J. Geophys. Res. Atmos. 98, 7265-7288.

Deplazes, G., Lückge, A., Peterson, L.C., Timmermann, A., Hamann, Y., Hughen, K.A., Röhl, U., Laj, C., Cane, M.A., Sigman, D.M., Haug, G.H., 2013. Links between tropical rainfall and North Atlantic climate during the last glacial period, Nat. Geosci., 6, 213-217.

Duplessy, J. C., Labeyrie, L., Arnold, M., Paterne, M., Duprat, J., van Weering, T.C.E., 1992. Changes in surface

salinity of the North Atlantic Ocean during the last deglaciation. Nature 358, 485-488.

Dykoski, C.A., Edwards, R.L., Cheng, H., Yuan, D.X., Cai, Y.J., Zhang, M.L., Lin, Y.S., Qing, J.M., An, Z.S., Revenaugh, J., 2005. A high-resolution, absolute-dated Holocene and deglacial Asian monsoon record from Dongge Cave, China. Earth Planet. Sc. Lett. 233, 71-86.

Fleitmann, D., Burns, S.J., Mangini, A., Mudelsee, M., Kramers, J., Villa, I., Neff, U., Al-Subbary, A.A., Buettner, A., Hippler, D., Matter, A., 2007. Holocene ITCZ and Indian monsoon dynamics recorded in stalagmites from Oman and Yemen (Socotra). Quat. Sci. Rev. 26, 170–188.

Fleitmann, D., Burns, S.J., Mudelsee, M., Neff, U., Kramers, J., Mangini, A., Matter, A., 2003. Holocene forcing of the Indian monsoon recorded in a stalagmite from southern Oman. Science 300, 1737–1739.

Fuchs, M., Buerkert, A., 2008. A 20 ka sediment record from the Hajar Mountain range in N-Oman, and its implication for detecting arid-humid periods on the southeastern Arabian Peninsula. Earth Planet. Sc. Lett. 265, 546-558.

Gasse, F., Fontes, J.C., van Campo, E., Wei, K., 1996. Holocene environmental changes in Bangong Co basin (Western Tibet). Part 4: Discussion and conclusions. Palaeogeogr. Palaeoclimatol. Palaeoecol. 120, 79–92.

Gayathri, N.M., Sijinkumar, A.V., Nath, B.N., Sandeep, K., Wei, K.Y., 2022. A ~ 30 kyr sub-centennial to millennial Indian summer monsoon variability record from the southern Andaman Sea, northeastern Indian Ocean. Palaeogeogr. Palaeoclimatol. Palaeoecol. 590, 110865.

Ge, Q.S., Hua, Z., Zheng, J.Y., Fang, X.Q., Xiao, L.B., Liu, J., Yang, B., 2015. Forcing and impacts of warm periods in the past 2000 years. Chin. Sci. Bull. 60, 1727-1734 (in Chinese).

Ge, Q.S., Liu, J., Fang, X.Q., Yang, B., Hao, Z.X., Shao, X.M., Zheng, J.Y., 2013. General characteristics of temperature change and centennial warm periods during the past 2000 years. Acta. Geographica. Sinica. 69, 579-592 (in Chinese).

Govil, P., Naidu, P.D., 2010. Evaporation - precipitation changes in the eastern Arabian Sea for the last 68 ka: Implications on monsoon variability. Paleoceanogr. Paleocl. 25, PA1210.

Govil, P., Naidu, P.D., 2011. Variations of Indian monsoon precipitation during the last 32 kyr reflected in the surface hydrography of the Western Bay of Bengal. Quat. Sci. Rev. 30, 3871-3879.

Griffiths, M.L., Drysdale, R.N., Gagan, M.K., Zhao, J.X., Ayliffe, L.K., Hellstrom, J.C., Hantoro, W.S., Frisia, S., Feng, Y.X., Cartwright, I., Pierre, E. ST., Fischer, M.J., Suwargadi, B.W., 2009. Increasing Australian–Indonesian monsoon rainfall linked to early Holocene sea-level rise. Nat. Geosci. 2, 636-639

Grinsted, A., Moore, J.C., Jevrejeva, S., 2004. Application of the cross wavelet transform and wavelet coherence to geophysical time series, Nonlin. Processes Geophys. 11, 561-566.

Grootes, P.M., Stuiver, M., 1997. Oxygen 18/16 variability in Greenland snow and ice with 10^{-3}- to 10^{5}-year time resolution. J. Geophy. Res.-Oceans 102, 26455-26470.

Grützner, J., Giosan, L., Franz, S.O., Tiedemann, R., Chaisson, W.P., Flood, R.D., Hagen, S., Keigwin, L.D., Poli, S., Rio, D., Williams, T., 2002. Astronomical age models for Pleistocene drift sediments from the western North Atlantic (ODP Sites 1053, 1063). Mar. Geol. 189, 5-23.

Gupta, A.K., Anderson, D.M., Overpeck, J.T., 2003. Abrupt changes in the Asian southwest monsoon during the Holocene and their links to the North Atlantic Ocean. Nature 421, 354-357.

Gupta, A.K., Das, M., Anderson, D.M., 2005. Solar influence on the Indian summer monsoon during the Holocene. Geophys. Res. Lett. 32, 1-4.

Hammer, Ø., Harper, D.A.T., Ryan, P.D., 2001. Past: Paleontological Statistics Software Package for Education and Data Analysis. Palaeont. Electron. 4, 9.

Herzschuh, U., Borkowski, J., Schewe, J., Mischke, S., Tian, F., 2014. Moisture-advection feedback supports strong early-to-mid Holocene monsoon climate on the eastern Tibetan Plateau as inferred from a pollen-based

reconstruction. Palaeogeogr. Palaeoclimatol. Palaeoecol. 402, 44-54.

Herzschuh, U., Winter, K., Wünnemann, B., Li, S.J., 2006. A general cooling trend on the central Tibetan Plateau throughout the Holocene recorded by the Lake Zigetang pollen spectra. Quatern. Int. 154-155, 113-121.

Hijmans, R.J., Cameron, S.E., Parra, J.L., Jones, P.G., Jarvis, A., 2005. Very high resolution interpolated climate surfaces for global land areas. Int. J. Climatol. 25, 1965-1978.

Hong, Y.T., Hong, B., Lin, Q.H., Zhu, Y.X., Shibata, Y., Hirota, M., Uchida, M., Leng, X.T., Jiang, H.B., Xu, H., Wang, H., Yi, L., 2003. Correlation between Indian Ocean summer monsoon and North Atlantic climate during the Holocene. Earth Planet. Sc. Lett. 211, 371-380.

Hu, F., Slawinski, D., Wright, H.E., Ito, E., Johnson, R.G., Kelts, K., McEwan, R.F., Boedigheimer, A., 1999. Abrupt changes in North American climate during Early Holocene times. Nature 400, 437-440.

Huang, C.J., Chang Y.T., Hsu, Y.C., Jen, H., 1998. Fagaceae. In: Chun, W.Y., Huang, C.C. eds. Flora of China (Vol. 22). Beijing: Science Press, pp. 213-332.

Huguet, C., Kim, J.H., Damsté, J.S.S., Schouten, S., 2006. Reconstruction of sea surface temperature variations in the Arabian Sea over the last 23 kyr using organic proxies (TEX^{86} and UK'^{37}). Paleoceanogr. Paleocl. 21, PA3003.

IPCC. Climate change 2013. The Physical Science Basis. Contribution of Working Group I to the Fifth Assessment Report of the Intergovernmental Panel on Climate Change. Cambridge University Press, Cambridge, United Kingdom and New York.

Jiang, W., Leroy, S.A.G., Yang, S., Zhang, E., Wang, L., Yang, X., Rioual, P., 2019. Synchronous strengthening of the Indian and East Asian monsoons in response to global warming since the last deglaciation. Geophys. Res. Lett. 46, 3944-3952.

Johnsen, S.J., Clausen, H.B., Dansgaard, W., Gundestrup, N.S., Hammer, C.U., Andersen, U., Andersen, K.K.,

Hvidberg, C.S., Dahl-Jensen, D., Steffensen, J.P., Shoji, H., Sveinbj¨ornsd´ottir, A.E., White, J., Jouzel, J., Fisher, D., 1997. The δ ^{18}O record along the Greenland Ice Core Project deep ice core and the problem of possible Eemian climatic instability. J. Geophys. Res. 102, 26397-26410.

Joussaume, S., Teylor, D., 1995. Status of the palaeoclimate modeling intercomparison project (PMIP). In Proceedings of the First International AMIP Science Conference, WCRP-92, Monterey, USA, pp. 425–430.

Juggins, S., 2013. Quantitative reconstructions in palaeolimnology: new paradigm or sick science? Quat. Sci. Rev. 64, 20-32.

Juggins, S., Birks, H.J.B., 2012. Quantitative enviornmental reconstructions from biological data. In: Birks, H.J.B., Lotter, A.F., Juggins, S., Smol, J.P. (Eds.), Tracking Environmental Change Using Lake Sediments vol. 5: Data Handling and Numerical Techniques. Springer Netherlands, Dordrecht, pp. 431–494.

Kaufman, D.S., McKay, N., Routson, C., Erb, M., Dätwyler, C., Sommer, P.S., Heiri, O., Davis, B., 2020. Holocene global mean surface temperature, a multi-method reconstruction approach. Sci. Data 7, 201.

Keeling, C.D., Whorf, T.P., 2000. The 1.800 year oceanic tidal cycle: A possible cause of rapid climate change. P. Natl. 97, 3814-3819.

Keigwin, L.D., Jones, G.A., 1994. Western North Atlantic evidence for millennial-scale changes in ocean circulation and climate. J. Geophys. Res.-Oceans 99, 12397-12410.

Kerr, R.A., 2005. Changes in the sun may sway the tropical monsoon. Science 308, 787.

Kessarkar, P.M., Rao, V.P., Naqvi, S.W.A., Karapurkar, S.G., 2013. Variation in the Indian Summer Monsoon intensity during the Bølling-Ållerød and Holocene. Paleoceanogr. Paleocl. 28, 413-425.

Kudrass, H.R., Hofmann, A., Doose, H., Emeis, K., Erlenkeuser, H., 2001. Modulation and amplification of climatic changes in the Northern Hemisphere by the Indian summer monsoon during the past 80 k.y., Geology, 29, 63-66.

Laskar, J., Robutel, P., Joutel, F., Gastineau, M., Correia, A.C.M., Levrard, B., 2004. A long term numerical solution for the insolation quantities of the Earth. Astronomy and Astro-Physics 428, 261–285.

Leuschner, D.C., Sirocko, F., 2003. Orbital insolation forcing of the Indian Monsoon-a motor for global climate changes? Palaeogeogr. Palaeoclimatol. Palaeoecol. 197, 83-95.

Liang, C., Zhao, Y., Qin, F., Zheng, Z., Xiao, X.Y., Ma, C.M., Li, H., Zhao, W.W., 2020. Pollen-based Holocene quantitative temperature reconstruction on the eastern Tibetan Plateau using a comprehensive method framework. Sci. China Earth Sci. 63, 1144-1160.

Liew, P.M., Lee, C.Y., Kuo, C.M., 2006. Holocene thermal optimal and climate variability of East Asian monsoon inferred from forest reconstruction of a subalpine pollen sequence, Taiwan. Earth Planet. Sc. Lett. 250, 596-605.

Liu, J.B., Chen, J.H., Zhang, X.J., Li, Y., Rao, Z.G., Chen, F.H., 2015. Holocene East Asian summer monsoon records in northern China and their inconsistency with Chinese stalagmite $\delta^{18}O$ records. Earth-Sci. Rev. 148, 194-208.

Liu, Z.Y., Zhu, J., Rosenthal, Y., Zhang, O.E., 2014. The Holocene temperature conundrum. Proc. Natl Acad. Sci. USA 111, E3501–E3505.

Lowe, J.J., Rasmussen S.O., Bjorck S, Hoek, W.Z., Steffensen, J.P., Walker, M.J.C., Yu, Z.C., the INTIMATE group, 2008. Synchronisation of palaeoenvironmental events in the North Atlantic region during the Last Termination: a revised protocol recommended by the INTIMATE group. Quat. Sci. Rev. 27, 6–17.

Lu, H., Wu, N., Liu, K.-b, Zhu, L., Yang, X., Yao, T., Wang, L., Li, Q., Liu, X., Shen, C., Li, X., Tong, G., Jiang, H., 2011. Modern pollen distributions in Qinghai-Tibetan Plateau and the development of transfer functions for reconstructing Holocene environmental changes. Quat. Sci. Rev. 30, 947-966.

MacFarling Meure, C., Etheridge, D., Trudinger, C., Steele, P., Langenfelds, R., van Ommen, T., Smith, A., Elkins,

J., 2006. The Law Dome CO_2, CH_4 and N_2O Ice Core Records Extended to 2000 years BP. Geophys. Res. Lett. 33, L14810.

Mann, M.E., Zhang, Z., Rutherford, S., Bradley, R.S., Hughes, M.K., Shindell, D., Ammann, C., Faluvegi, G., Ni, F., 2009. Global Signatures and Dynamical Origins of the Little Ice Age and Medieval Climate Anomaly. Science 326, 1256-1260.

Marcott, S.A., Shakun, J.D., Clark, P.U., Mix, A.C., 2013. A Reconstruction of Regional and Global Temperature for the Past 11,300 Years. Science 339, 1198-1201.

Mayewski, P.A., Meeker, L.D., Twickler, M.S., Whitlow, S., Yang, Q.Z Lyons, W.B., Prentice, M., 1997. Major features and forcing of high latitude Northern Hemisphere atmospheric circulation using 110,000-year-long glaciochemical record. J. Geophys. Res.-Oceans 102, 26345-26366.

Mayewski, P.A., Rohling, E.E., Stager, J.C., Karlén, W. Maasch, K.A., Meyerson, E.A., Gasse, F., van Kreveld, S., Holmgren, K., Lee-Thorp, J., Rosqvist, G., Rack, F., Stabwasser, M., Schneider, R.R., Rack, F., Staubwasser, M., Schneider, R.R., Steig, E.J., 2004. Holocene climate variability. Quat. Res. 62, 243-255.

Mohtadi, M., Prange, M., Oppo, D., De Pol-Holz, R., Merkel, U., Zhang, X., Stephan, S., Lückge, A., 2014. North Atlantic forcing of tropical Indian Ocean climate. Nature 509, 76-80.

Monnin, E., Indermuhle, A., Dallenbach, A., Fluckiger, J., Stauffer, B., Stocker, T.F., Raynaud, D., Barnola, J.M., 2001. Atmospheric CO_2 concentrations over the last glacial termination. Science 291, 112-114.

Moros, M., Deckker, P.D., Jansen, E., Perner, K., Telford, R.J., 2009. Holocene climate variability in the Southern Ocean recorded in a deep-sea sediment core off South Australia. Quat. Sci. Rev. 28, 1932-1940.

Naidu, P.D., Malmgren, B.A., 2005. Seasonal sea surface temperature contrast between the Holocene and last glacial period in the western Arabian Sea (Ocean drilling project site 723A): modulated by monsoon upwelling. Paleoceanogr. Paleocl. 20, PA1004.

Nakamura, A., Yokoyama, Y., Maemoku, H., Yagi, H., Okamura, M., Matsuoka, H., Miyake, N., Osada, T., Adhikari, D.P., Dangol, V., Ikehara, M., Miyairi, Y., Matsuzaki, H., 2016. Weak monsoon event at 4.2 ka recorded in sediment from Lake Rara, Himalayas. Quatern. Int. 397, 349-359.

Neff, U., Burns, S.J., Mangini, A., Mudelsee, M., Fleitmann, D., Matter, A., 2001. Strong coherence between solar variability and the monsoon in Oman between 9 and 6 kyr ago. Nature 411, 290-293.

Ng, H.C., Robinson, L.F., McManus, J.F., Mohamed, K.J., Jacobel, A.W., Ivanovic, R.F., Gregoire, L.J., Chen, T.Y., 2018. Coherent deglacial changes in western Atlantic Ocean circulation. Nat. Commun. 9, 2947.

Nychka, D., Furrer, R., Paige, J., Sain, S., Gerber, F., Iverson, M., 2020. fields: Tool for Spatial Data.

Opitz, S., Zhang, C.J., Herzschuh, U., Mischke, S., 2015. Climate variability on the south-eastern Tibetan Plateau since the Lateglacial based on a multiproxy approach from Lake Naleng - comparing pollen and non-pollen signals. Quat. Sci. Rev. 115, 112-122.

Overpeck, J., Anderson, D., Trumbore, S., Prell, W., 1996. The Southwest Indian Monsoon over the last 18000 years. Clim. Dynam. 12, 213-225.

Peltier, W.R., Fairbanks, R.G., 2006. Global glacial ice volume and Last Glacial maximum duration from an extended Barbados sea level record. Quat. Sci. Rev. 25, 3322-3337.

Pestiaux, P., Van Der Mersch, I., Berger, A., Duplessy, J.C., 1988. Paleoclimatic variability at frequencies ranging from 1 cycle per 10,000 years to 1 cycle per 1000 years: Evidence for nonlinear behaviour of the climate system. Climatic Change 12, 9-37.

Rao, Z.G., Li, Y.X., Zhang, J.W., Jia, G.D., Chen, F.H., 2016. Investigating the long-term palaeoclimatic controls on the δ D and δ ^{18}O of precipitation during the Holocene in the Indian and East Asian monsoonal regions. Earth-Sci. Rev. 159, 292-305.

Ruddiman, W.F., 2003. The anthropogenic greenhouse era began thousands of years ago. Climatic Change 61,

261-293.

Seppä, H., Birks, H.J.K., Odland, A., Poska, A., Veski, S., 2004. A modern pollen–climate calibration set from northern Europe: developing and testing a tool for palaeoclimatological reconstructions. J. Biogeogr. 31, 251-267.

Shakun, J.D., Carlson, A.E., 2010. A global perspective on Last Glacial Maximum to Holocene climate change. Quat. Sci. Rev. 29, 1801-1816.

Shen, C., Liu, K.-b., Morrill, C., Peng, J., Overpeck, J.T., Tang, L., 2008. Ecotone shift and major droughts during mid-late Holocene in central Tibetan Plateau. Ecology 89, 1079-1088.

Shen, C., Liu, K.-b., Tang, L., Overpeck, J.T., 2006. Quantitative relationships between modern pollen rain and climate in the Tibetan Plateau. Rev. Paleobot. Palyno. 140, 61-77.

Siddall, M., Rohling, E.J., Almogi-Labin, A., Hemleben, Ch., Meischner, D., Schmelzer, I., Smeed, D.A., 2003. Sea-level fluctuations during the Last Glacial cycle. Nature 423, 853-858.

Sonzogni, C., Bard, E., Rostek, F., 1998. Tropical sea-surface temperatures during the last glacial period: A view based on alkenones in Indian Ocean sediments. Quat. Sci. Rev. 17, 1185-1201.

Soon, W., Baliunas, S., Idso, C., Idso, S., Legates, D., 2003. Reconstructing climatic and environmental changes of the past 1000 years: A reappraisal. Energy Environ. Sci. 14, 233-296.

Staubwasser, M., Sirocko, F., Grootes, P. M., Erlenkeuser, H., 2002. South Asian monsoon climate change and radiocarbon in the Arabian Sea during early and middle Holocene. Paleoceanogr. Paleocl. 17, 1063.

Steinhilber, F., Abreu, J.A., Beer, J., Brunner, I., Christl, M., Fischer, H., Heikkilä, U., Kubik, P.W., Mann, M., McCracken, K.G., Miller, H., Miyahare, H., Oerter, H., Wilhelms, F., 2012. 9,400 years of cosmic radiation and solar activity from ice cores and tree rings. P. Natl. Acad. Sci. USA, 109, 5967-5971.

Stuiver, M., Braziunas, T.F., 1989. Atmospheric ^{14}C and century scale solar oscillations. Nature 338: 405-408.

Stuiver, M., Braziunas, T.F., 1993. Sun, ocean, climate and atmospheric 14CO2: an evaluation of causal and spectral relationships. Holocene 3, 289-305.

Stuiver, M., Grootes, P.M., Braziunas, T.F., 1995: The GISP2 $\delta^{18}O$ climate record of the past 16,500 years and the role of the sun, ocean and volcanoes, Quat. Res. 44, 341-54.

Suess, H.E., 1980. The radiocarbon record in tree rings of the last 8000 years. Radiocarbon 22, 200-209.

Sun, X.S., Zhao, C., Zhang, C., Feng, X.P., Yan, T.L., Yang, X.D., Shen, J., 2021. Seasonality in Holocene temperature reconstructions in southwestern China. Paleoceanogr. Paleoclim. 36, e2020PA004025.

Telford, R.J., Birks, H.J.B., 2005. The secret assumption of transfer functions: problems with spatial autocorrelation in evaluating model performance. Quat. Sci. Rev. 24, 2173–2179.

Telford, R.J., Birks, H.J.B., 2011. A novel method for assessing the statistical significance of quantitative reconstructions inferred from biotic assemblages. Quat. Sci. Rev. 30, 1272-1278.

ter Braak, C.J.F., 1988. CANOCO-a FORTRAN Program for Canonical Community Ordination by [Partial] [Detrended] [Canonical] Correspondence Analysis, Principal Components Analysis and Redundancy Analysis Version 2.1. Agricultural Mathematics Group, Wageningen, The Netherlands.

ter Braak, C.J.F., Prentice, I.C., 1988. A theory of gradient analysis. Adv. Ecol. Res. 34, 235–282.

ter Braak, C.J.F., Šmilauer, P., 2012. Canoco reference manual and user's guide: software for ordination, version 5.0. Ithaca USA: Microcomputer Power, Ithaca, New York.

Thamban, M., Kawahata, H., Rao, V.P., 2007. Indian Summer Monsoon Variability during the Holocene as Recorded in Sediments of the Arabian Sea: Timing and Implications. J. Oceanogr. 63, 1009-1020.

Thompson, A.J., Zhu, J., Poulsen, C.J., Tierney, J.E., Skinner, C.B., 2022. Northern Hemisphere vegetation change drives a Holocene thermal maximum. Sci. Adv. 8, eabj6535.

Thompson, L.G., Mosley-Thompson, E., Davis, M.E., Henderson, K.A., Brecher, H.H., Zagorodnov, V.S.,

Mashiotta, T.A., Lin, P.N., Mikhalenko, V.N., Hardy, D.R., Beer, J., 2002. Kilimanjaro ice core records: evidence of Holocene climate change in tropical Africa. Science 298, 589-593.

Tian, L.P., Wang, M.Y., Zhang, X., Yang, X.Q., Zong, Y.Q., Jia, G.D., Zheng, Z., Man, M.L., 2019. Synchronous change of temperature and moisture over the past 50 ka in subtropical southwest China as indicated by biomarker records in a crater lake. Quat. Sci. Rev. 212, 121-134.

Tiwari, M., Ramesh, R., Somayajulu, B.L.K., Jull, A.J.T., Burr G.S., 2005. Solar control of southwest monsoon on centennial timescales. Curr. Sci. India 89, 1583-1588.

Usoskin, I.G., Mursula, K., 2003. Long-term solar cycle evolution: Review of recent developments. Sol. Phys. 218, 319-343.

Waelbroeck, C., Duplessy, J.C., Michel, E., Labeyrie, L., Paillard, D., Duprat, J., 2001. The timing of the last deglaciation in North Atlantic climate records. Nature 412, 724-727.

Wang, D.D., Li, M.Y., Zhang, S.R., Xu, Q.H., Wu, L.W., 2022. Spatial and temporal characteristics of the precipitation response to the 4.2 ka event in the Asian summer monsoon region. Global Planet. Change 214, 103854.

Wang, G., Wang, R.L., Wu, Z.F., He, W., Ma, X.Y., Zhang, T., 2021. Reconstruction of temperature and precipitation spanning the past 28 kyr based on branched tetraether lipids from Qionghai Lake, southwestern China. Palaeogeogr. Palaeoclimatol. Palaeoecol. 562, 110094.

Wang, X.F., Edwards, R.L., Auler, A.S., Cheng, H., Ito, E., 2007. Millennial-scale interhemispheric asymmetry of low-latitude precipitation: Speleothem evidence and possible high-latitude forcing, in Schmittner, A., et al., eds., Ocean circ. Mech. Impacts-Past futur. Chang. Merid. Overturning 173, 279–294.

Wang, Y.F., Zhu, Y.X., Pan, H.X., Yin, Y., 2002. Environmental characteristics of an acid Qinghai Lake in Tengchong, Yunnan Province. J. Lake Sci. 14, 117-124 (in Chinese).

Wang, Y.J., Cheng, H., Edwards, R.L., An, Z.S., Wu, J.Y., Shen, C.C., Dorale, J.A., 2001. A high-resolution absolute-dated late Pleistocene monsoon record from Hulu Cave, China. Science 294, 2345-2348.

Wang, Y.J., Cheng, H., Edwards, R.L., He, Y.Q., Kong, X.G., An, Z.S., Wu, J.Y., Kelly, M. J., Dykoski, C.A., Li, X.D., 2005. The Holocene Asian monsoon: links to solar changes and North Atlantic climate. Science 308, 854-857.

Webb, T., Bryson, R.A., 1972. Late- and post-glacial climate change in Northern Midwest, USA: quantitative estimates derived from fossil pollen spectra by multivariate statistical analysis. Quat. Res. 2, 70-115.

Wright, H.E., Kutzbach, J.E., Webb III, T., Ruddiman, W.F., Street-Perrott, F.A., Bartlein, P.J., (Eds.), 1993. Global Climates since the Last Glacial Maximum. University of Minnesota Press, Minneapolis, MN, pp. 569.

Wu, D., Chen, X.M., Lv, F.Y., Brenner, M., Curtis, J., Abbott, M., Yu, J.Q., Chen, F.H., 2018. Decoupled early Holocene summer temperature and monsoon precipitation in southwest China. Quat. Sci. Rev. 193, 54-67.

Wu, Y., Li, T.Y., Yu, T.L., Shen, C.C., Chen, C.J., Zhang, J., Li, J.Y., Wang, T., Huang, R., Xiao, S.Y., 2020. Variation of the Asian summer monsoon since the last glacial-interglacial recorded in a stalagmite from southwest China. Quat. Sci. Rev. 234, 106261.

Xiao, X.Y., Haberle, S.G., Li, Y.L., Liu, E.F., Shen, J., Zhang, E.L., Yin, J.J., Wang, S.M., 2018. Evidence of Holocene climatic change and human impact in northwestern Yunnan Province: High-resolution pollen and charcoal records from Chenghai Lake, southwestern China. Holocene 28, 127-139.

Xiao, X.Y., Haberle, S.G., Shen, J., Yang, X.D., Han, Y., Zhang, E.L., Wang, S.M., 2014a. Latest Pleistocene and Holocene vegetation and climate history inferred from an alpine lacustrine record, northwestern Yunnan Province, southwestern China, Quat. Sci. Rev. 86, 35-48.

Xiao, X.Y., Haberle, S.G., Yang, X.D., Shen, J., Han, Y., Wang, S.M., 2014b. New evidence on deglacial climatic variability from an alpine lacustrine record in northwestern Yunnan Province, southwestern China.

Palaeogeogr. Palaeoclimatol. Palaeoecol. 406, 9-21.

Xiao, X.Y., Shen, J., Haberle, S.G., Xue, B., Zhang, E.L., Wang, S.M., Tong, G.B., 2015. Vegetation, fire, and climate history during the last 18500 years in southwestern Yunnan Province of China. J. Quat. Sci. 30, 859-869.

Xu, D.K., Lu, H.Y., Chu, G.Q., Wu, N.Q., Shen, C.M., Wang, C., Mao, L.M., 2014. 500-year climate cycles stacking of recent centennial warming documented in an East Asian pollen record. Sci. Rep.-UK 4, 3611.

Yan, T.L., Zhao, C., Yan, H., Shi, G., Sun, X.S., Zhang, C., Feng, X.P., Leng, C.S., 2021. Elevational differences in Holocene thermal maximum revealed by quantitative temperature reconstructions at ~30º N on eastern Tibetan Plateau. Palaeogeogr. Palaeoclimatol. Palaeoecol. 570, 110364.

Yang, S.L., Dong, X.X., Xiao, J.L., 2018. The East Asian Monsoon since the Last Glacial Maximum: Evidence from geological records in northern China. Sci. China Earth Sci. 61, 1-12.

Yang, Y., Zhang, H., Chang, F., Meng, H., Dan, A., Zheng, Z., Rong, X., 2016. Vegetation and climate history inferred from a Qinghai Crater Lake pollen record from Tengchong, southwestern China. Palaeogeogr. Palaeoclimatol. Palaeoecol. 461, 1-11.

Yasuhara, M. deMenocal, P.B., Dwyer, G.S., Cronin, T.M., Okahashi, H., May Huang, H.-H., 2019. North Atlantic intermediate water variability over the past 20,000 years. Geology, 47, 659-663.

Yi, S., Saito, Y., Zhao, Q., Wang, P.X., 2003. Vegetation and climate changes in the Changjiang (Yangtze River) Delta, China, during the past 13,000 years inferred from pollen records. Quat. Sci. Rev. 22, 1501-1519.

Yiou, P., Genthon, C., Jouzel, J., Treut, H.L., Barnola, J.M., Lorius, C., Korotkevitch, Y.N., 1991. High-frequency paleovariability in climate and in CO2 levels from Vostok ice-core records. J. Geophys. Res.-Oceans 96, 20365-20378.

Yiou, P., Jouzel, J., Johnsen, S., Rögnvaldsson, Ö.E., 1995. Rapid oscillations in Vostok and GRIP ice cores.

Geophys. Res. Lett. 22, 2179-2182.

Zhang, C., Zhao, C., Yu, S.Y., Yang, X.D., Cheng, J., Zhang, X.J., Xue, B., Shen, J., Chen, F.H., 2022. Seasonal imprint of Holocene temperature reconstruction on the Tibetan Plateau. Earth-Sci. Rev. 226, 103927.

Zhang, E.L., Chang, J., Cao, Y.M., Sun, W.W., Shulmeister, J., Tang, H.Q., Langdon, P.G., Yang, X.D., Shen, J., 2017. Holocene high-resolution quantitative summer temperature reconstruction based on subfossil chironomids from the southeast margin of the Qinghai-Tibetan Plateau. Quat. Sci. Rev. 165, 1-12.

Zhang, E.L., Chang, J., Shulmeister, J., Langdon P., Sun, W.W., Cao, Y.M., Tang, X.D., Shen, J., 2019. Summer temperature fluctuations in Southwestern China during the end of the LGM and the last deglaciation. Earth Planet. Sc. Lett. 509, 78-87.

Zhang, W.C., Wu, H.B., Cheng, J., Geng, J.Y., Li, Q., Sun, Y., Yu, Y.Y., Lu, H.Y., Guo, Z.T., 2022. Holocene seasonal temperature evolution and spatial variability over the Northern Hemisphere landmass. Nat. Commun.13, 5334.

Zhang, X., Zheng, Z., Huang, K., Cheng, J., Cheddadi, R., Zhao, Y., Liang, C., Yang, X., Wan, Q., Tang, Y., Chen, C., Li, J., 2023. Quantification of Asian monsoon variability from 68 ka BP through pollen-based climate reconstruction. Sci. Bull. 68, 713-722.

Zhang, X., Zheng, Z., Huang, K., Yang, X., Tian, L., 2020. Sensitivity of altitudinal vegetation in southwest China to changes in the Indian summer monsoon during the past 68000 years. Quat. Sci. Rev. 239, 1-16.

Zhao, C., Rohling, E.J., Liu, Z.Y., Yang, X.Q., Zhang, E.L., Cheng, J., Liu, Z.H., An, Z.S., Yang, X.D., Feng, X.P., Sun, X.S., Zhang, C., Yan, T.L., Long, H., Yan, H., Yu, Z.C., Liu, S.Y., Shen, J., 2021. Possible obliquity-forced warmth in southern Asia during the last glacial stage. Sci. Bull. 66, 1136–1145.

Zhao, Y., Liang, C., Cui, Q.Y., Qin, F., Zheng, Z., Xiao, X.Y., Ma, C.M., Felde, V.A., Liu, Y.L., Li, Q., Herzschuh, U., Xu, Q.H., Wei, H.C., Cai, M.T., Cao, X.Y., Guo, Z.T., Birks, H.J.B., 2021. Temperature reconstructions

for the last 1.74-Ma on the eastern Tibetan Plateau based on a novel pollen-based quantitative method. Global Planet. Change 199, 103433.

Zhou, Z.K., Yang, Q.S., Xia, K., 2007. Fossils of *Quercus sect. Heterobalanus* can help explain the uplift of the Himalayas. Chin. Sci. Bull. 52, 238-247.

Zielinski, G.A., Mershon, G.R., 1997. Paleoenvironmental implications of the insoluble microparticle record in the GISP2 (Greenland) ice core during the rapidly changing climate of the Pleistocene-Holocene transition. Geol. Soc. Am. Bull. 109, 547–559.

Declaration of interests

The authors declare that they have no known competing financial interests or personal relationships that could have appeared to influence the work reported in this paper.

Highlights:

We present high-resolution pollen-based quantitative variations in MTCM, MAT and MAP from southwestern China.
The period 7.2-4.5 ka was the warmest and wettest period since 18.5 ka.
Seven abrupt cold and dry events were detected over the past 18.5 ka.
This study provides quantitative data support for ecological responses and climate mechanisms.